Role of Base Sequence Context in Conformational Equilibria and Nucleotide Excision Repair of Benzo[*a*]pyrene Diol Epoxide−Adenine Adducts†

Shixiang Yan,‡ Min Wu,‡ Tonko Buterin,§ Hanspeter Naegeli,§ Nicholas E. Geacintov,*,‡ and Suse Broyde*,||

Department of Chemistry, New York University, New York, New York 10003, Institute of Pharmacology and Toxicology, University of Zürich-Tierspital, CH-8008 Zürich, Switzerland, and Department of Biology, New York University, New York, New York 10003

Received October 15, 2002; Revised Manuscript Received December 20, 2002

ABSTRACT: We investigate the influence of base sequence context on the conformations of the 10*S* (+)- and 10*R* (−)-*trans*-*anti*-[BP]-N^6-dA adducts through molecular dynamics (MD) simulations with free energy calculations, and relate the structural findings to results of nucleotide excision repair (NER) assays in human cell extracts. In previous studies, these adducts were studied in the CA*A sequence context, and here we report results for the CA*C sequence. Our simulations indicate that the base sequence context affects the *syn*−*anti* conformational equilibrium in the 10*S* (+) adduct by modulating the barrier heights between these states on the energy surface, with a higher barrier in the CA*C case. Our nucleotide excision repair assay finds greater NER susceptibilities in the 10*S* (+) adduct for the CA*C sequence context. A structural rationale ties together these results. A sequence specific hydrogen bond, accompanied by a significantly increased roll and consequent bending in the 10*S* (+) adduct, has been found in our simulations for the CA*C sequence, which could account for the enhanced nucleotide excision repair as well as the *syn*−*anti* equilibrium difference we observe in this isomer and sequence. Such sequence specific differential repair could contribute to the existence of mutational hotspots and thereby contribute to the complexity of cancer initiation.

The mutagenic consequences of DNA bases chemically modified by reaction with bulky substituents such as polynuclear aromatic derivatives are strongly influenced by the base sequence context surrounding the damaged base (*1*−*9*). If these covalent adducts are not excised by the nucleotide excision repair (NER)[1] machinery, processing of the lesions by DNA polymerases may lead to mutation (*10*−*18*), which can ultimately give rise to cancer (*19, 20*). Such mutagenic processing of bulky adducts by polymerases likely depends on the conformation of the adduct. The possibility that the conformation of a given adduct may depend on base sequence context has been a subject of considerable interest (*21*−*23*). Furthermore, different adduct conformers may be interconvertible in certain sequence contexts, thus perhaps facilitating mutagenic polymerase bypass when the adducts assume an appropriate conformational state.

Clear evidence for conformational heterogeneity governed by base sequence context has been obtained in the case of DNA adducts derived from metabolically activated benzo[*a*]pyrene (BP), including the *syn*- and *anti*-benzo[*a*]pyrene diol epoxides (BPDEs) (*24*). These *syn*- and *anti*-BPDEs can react with purines in DNA by *cis*- and *trans*-epoxide opening to yield covalent adducts (*25*−*27*). In the case of the 10*S* (+)-*trans*-*anti*-[BP]-N^2-dG adduct, high-resolution NMR solution data revealed a single conformer, with the BP moiety in the minor groove directed toward the 5′-end of the modified strand in the CG*C sequence context. (The asterisk following the base designates carcinogen modification.) In the TG*C sequence (*28*), the same conformer was also observed as the major form, but a minor conformer of unspecified structure in equilibrium with the major one was also evident. Furthermore, with T's flanking the same modified guanine on both sides, significant conformational heterogeneity was observed in this TG*T sequence context, which precluded a structural characterization of the 10*S* (+)-*trans*-*anti*-[BP]-N^2-dG adduct in this case (*29*).

Conformational adduct heterogeneity is also pronounced in the case of adenine adducts derived from BPDEs, the [BP]-N^6-dA lesions (Figure 1). In the CA*C sequence context of the 10*S* (+)-*trans*-*syn*-[BP]-N^6-dA adduct, both a major and a minor conformer were characterized in a fully complementary duplex with a T opposite the modified adenine base. However, in the case of the stereoisomeric 10*S* (+)-*trans*-*anti*-[BP]-N^6-dA adduct, also in a CA*C sequence context,

† This research is supported by NIH Grant CA-28038 to S.B., NIH Grant CA-76660 to N.E.G., and Swiss National Science Foundation Grant 31-61494.00 to H.N.

* To whom correspondence should be addressed. N.E.G.: telephone, (212) 998-8407; fax, (212) 998-8421; e-mail, ng1@nyu.edu. S.B.: telephone, (212) 998-8231; fax, (212) 995-4015; e-mail, broyde@nyu.edu.

‡ Department of Chemistry, New York University.

§ University of Zürich-Tierspital.

|| Department of Biology, New York University.

[1] Abbreviations: (+)-*anti*-BPDE, (+)-(7*R*,8*S*,9*S*,10*R*)-7,8-dihydroxy-9,10-epoxy-7,8,9,10-tetrahydrobenzo[*a*]pyrene; (−)-*anti*-BPDE, (−)-(7*S*,8*R*,9*R*,10*S*)-7,8-dihydroxy-9,10-epoxy-7,8,9,10-tetrahydrobenzo[*a*]-pyrene; (+)-*syn*-BPDE, (+)-(7*S*,8*R*,9*S*,10*R*)-7,8-dihydroxy-9,10-epoxy-7,8,9,10-tetrahydrobenzo[*a*]pyrene; BP, benzo[*a*]pyrene; BPDE, benzo-[*a*]pyrene diol epoxide; HPLC, high-performance liquid chromatography; MD, molecular dynamics; MM-PBSA, molecular mechanics Poisson−Boltzmann surface area; NER, nucleotide excision repair; NMR, nuclear magnetic resonance; RESP, restrained electrostatic potential fitting; rmsd, root-mean-square deviation; ROESY, rotating-frame Overhauser effect spectroscopy; SASA, solvent-accessible surface area.

10.1021/bi0270081 CCC: $25.00
Published on Web 02/07/2003

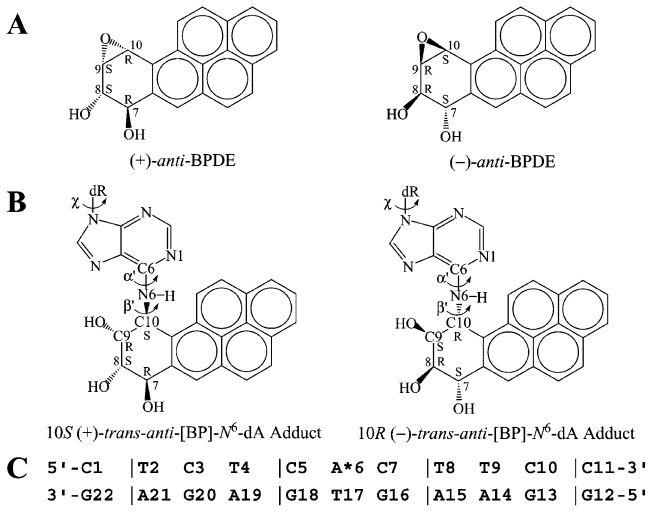

FIGURE 1: Structures of (A) (+)- and (−)-*anti*-BPDE and (B) 10*S* (+)- and 10*R* (−)-*trans-anti*-[BP]-N^6-dA adducts. Torsion angles α′ and *β*′ are defined as follows: α′, N1−C6−N6−C10(BP); *β*′, C6−N6−C10(BP)−C9(BP). (C) Oligonucleotide sequence employed in the MD simulations. A*6 is the modified adenine residue.

it was not possible to fully characterize the structure of this adduct because there were several interconverting conformers when a T was positioned in the complementary strand opposite the BP-modified adenine. However, when the T, opposite the same 10*S* (+)-*trans-anti*-[BP]-N^6-dA adduct, was replaced with a G opposite the lesion, two different intercalated conformers could be discerned (*30*, *31*). Both conformers had the BP moiety intercalated on the 3′-side of the modified base, but the glycosidic torsion angle of the modified adenine was in the *syn* domain in the major conformer and in the *anti* domain in the minor one. Attempts have been made to determine the structure of the 10*S* (+)-*trans-anti*-[BP]-N^6-dA adduct with the complementary T opposite the lesion in the CA*A and AA*G sequence contexts as well, but the attempts failed because of adduct heterogeneities (*31*−*33*). However, in the case of the stereoisomeric 10*R* (−)-*trans-anti*-[BP]-N^6-dA adduct with T opposite the adducts, it was possible to determine high-resolution NMR solution structures in the CA*A, CAA*, and AA*G sequence contexts (*32*−*34*). Also, a high-resolution NMR structure has been obtained for the 10*R* (+)-*cis-anti*-[BP]-N^6-dA adduct with T opposite the lesion in the CA*C sequence context (*35*). In all cases with the *R* absolute adduct configuration, the BP ring system is intercalated on the 5′-side of the modified adenine base with an *anti* glycosidic torsion conformation. However, evidence for conformational equilibria between *syn* and *anti* glycosidic bond conformations was obtained for the AA*G sequence context, although the structure of the minor *syn* conformer could not be fully characterized (*33*). Also, a C3′-*endo*−C2′-*endo* equilibrium in the sugar conformation at A, 5′ to the modified A*, in the CAA* sequence context was found by Zegar et al. (*32*) for this adduct. The same possibility was also considered by Volk et al. (*33*). Clearly, as noted by Volk et al. (*33*), "the role of sequence in promoting such dynamic behavior is at present a fascinating, but open, question" for benzo[*a*]pyrene-derived adducts. For adducts derived from aromatic amines, such base sequence effects have been clearly delineated (*23*).

Our objectives are to utilize molecular dynamics (MD) simulations with free energy calculations to investigate the structural and thermodynamic factors that play important roles in determining the conformational properties of the adducts, and to relate these to their biological properties (*36*−*38*). In this paper, we investigate the sequence dependence of the *syn*−*anti* conformational equilibrium and its possible relationship to NER. We compare the conformational characteristics of the 10*S* (+)- and 10*R* (−)-*trans-anti*-[BP]-N^6-dA adducts (Figure 1) in the CA*A sequence context studied previously (*36*), with the CA*C sequence investigated here. We find an interesting influence of base sequence context on the *syn*−*anti* conformational equilibrium in the 10*S* (+) isomer, involving a difference in barrier heights between these states in the two sequences, with a higher barrier in the CA*C case. Using human cell extracts, we also investigate nucleotide excision repair of these adducts in the CA*C sequence and compare the results with those of a previous study in the CA*A sequence (*39*). We find enhanced excision for the 10*S* (+) isomer in the CA*C sequence. A structural rationale ties together these results. A sequence specific hydrogen bond, accompanied by significantly increased roll and consequent bending in the 10*S* (+) isomer, found in our simulations for the CA*C sequence could account for the enhanced nucleotide excision repair observed in this isomer and sequence, as well as for the *syn*−*anti* equilibrium difference.

MATERIALS AND METHODS

Starting Structures and Force Field. Our studies were carried out for the duplex 11-mer in the d(CTCTCA*CTTCC)·d(GGAAGTGAGAG) sequence context (Figure 1). We employed NMR solution structures in different sequence contexts as starting models for our simulations, since NMR structures for our sequence were not available. Specifically, for the 10*R* (−)-*trans-anti*-[BP]-N^6-dA adduct, we employed one starting structure with an *anti* glycosidic conformation and a normal partner T opposite the lesion (PDB entry 1AGU) (*34*, *40*). For the 10*S* (+)-*trans-anti*-[BP]-N^6-dA adduct, two starting structures were used (PDB entries 1BPS and 1DXA), which contain the modified adenine in the *anti* and *syn* glycosidic conformations, respectively, and have a mismatched G opposite the lesion (*30*, *31*). We remodeled all the structures to our current sequence context with Insight II 97.0 from Accelrys Inc., a subsidiary of Pharmacopeia, Inc., using the modeling procedure described previously (*36*). The starting structure for the unmodified d(CTCTCACTTCC)·d(GGAAGTGAGAA) DNA duplex was an energy-minimized B-form DNA computed with DUPLEX (*41*) from a B-DNA fiber diffraction model (*42*).

To obtain partial charges for the 10*S* (+)- and 10*R* (−)-*trans-anti*-[BP]-N^6-dA nucleosides, we excised them from the NMR duplex DNA structures (*30*, *31*, *43*), minimized them, and used Hartree−Fock calculations with the 6-31G* basis set to calculate the electrostatic potential, using Gaussian 94 (*44*). The charge was then fitted to each atomic center with restrained electrostatic potential fitting (RESP) (*45*). These partial charges were then normalized to maintain a charge of −1 on the modified nucleotide, using our previously described protocol (*46*). Bond angle parameters added to the force field for the two adducts, assigned by analogy to chemically similar atom types already available

in the *parm98* parameter set (*47*), are the same as those given previously (*36*).

Molecular Dynamics Protocol and Free Energy Analysis. Molecular dynamics simulations were carried out using the AMBER 5.0 package (*48*) with the Cornell et al. force field (*49*) and the *parm98* parameter set (*47*). The particle mesh Ewald (PME) method (*50*, *51*) was used to treat long-range electrostatic interactions with a cubic B-spline interpolation and a 10^{-5} tolerance for the direct space sum cutoff. A 12 Å cutoff was applied to the nonbonded Lennard-Jones interactions. The SHAKE algorithm (*52*) was applied to constrain all bonds involving hydrogen atoms with a tolerance of 0.0005 Å, and a time step of 1 fs was used in the dynamics simulations. The translational motion of the center of mass was removed approximately every 300 ps. Removal of the global rotational motion in a periodic system is technically uncertain and hence was not implemented. However, visual inspection of the trajectories revealed no abnormal overall rotation of the DNA duplexes, indicating that energy leakage from internal motion to global rotation through the "flying ice cube effect" (*53*) is not contributing in this case. In all, 20 Na^+ ions were added to the system for neutralization using the *LEap* module in AMBER 5.0. The system was then solvated with a rectangular box of TIP3P waters (*54*) which extended ~10 Å from the DNA atoms in each direction. This yields a periodic box size of ~52 Å × ~52 Å × ~65 Å for the 10*S* (+) and 10*R* (−) adducts and the unmodified control. In all, 4635 water molecules were added for the 10*S* (+) adduct, 4068 for the 10*R* (−) adduct, and 3529 for the unmodified control. All systems followed the same minimization and equilibration protocols, and these were the same as those employed in our earlier work (*36*) on the CA*A sequence context. First, the water molecules and counterions were minimized for 1500 steps of steepest descent, followed by 50 ps of dynamics with the DNA fixed to allow the solvent to relax. The whole system was then minimized for 1000 additional steps of steepest descent, followed by 3 ps of dynamics with 25 kcal/mol restraints on the DNA, which further allowed the waters to relax. Then the system was minimized for five rounds of 600 steps of steepest descent with the restraints on the DNA reduced by 5 kcal/mol each round, from 20 to 0 kcal/mol. Finally, the whole system was heated from 10 to 300 K over the course of 40 ps using the Berendsen coupling algorithm (*55*) with a coupling parameter of 0.2 ps. Production simulation was then continued at atmospheric pressure with a 0.2 ps coupling parameter and 300 K for 2.5 ns. All systems exhibited reasonably stable oscillations over the 2.5 ns simulation, as shown by the time dependence of the root-mean-square deviations (rmsd) (Figure S1 of the Supporting Information). Helicoidal parameters and DNA backbone torsion angles were computed using Dials and Windows (*56*). Hydrogen bond occupancies were computed using the MOIL-View program (*57*). To quantitatively assess the DNA helical bending, one base pair at each end of the DNA duplex was first truncated to avoid possible end effects, and then the overall axis bend angles were computed using the CURVES program (*58*), employing the "PP" option, which yields a bend angle measured between the vectors composed of the first two and last two reference points defining the axis.

MM-PBSA free energy analyses were carried out using the exact protocol described in detail in our earlier work (*36*). In brief, the free energy (G_{tot}) was computed from the molecular mechanical energies (E_{MM}), the solvation free energy ($G_{solvation}$), and the solute entropic contributions to the free energy ($\Delta G_{tot} = \Delta E_{MM} + \Delta G_{solvation} - T\Delta S$). The molecular mechanical energies (E_{MM}) were calculated from internal energies (E_{int}) stemming from deviations of the bonds (E_{bonds}), angles (E_{angles}), and dihedral angles ($E_{dihedrals}$) from their equilibrium values, the van der Waals energies (E_{vdW}), and electrostatic energies ($E_{electrostatic}$). The solvation free energies ($G_{solvation}$) were estimated from the electrostatic solvation energies (G_{PB}) calculated using the DelPhi program (*59*, *60*) and the nonpolar solvation energy ($G_{nonpolar}$); the latter was approximated as $G_{nonpolar} = \gamma S_A + b$ ($\gamma = 0.00542$ kcal/Å^2, $b = 0.92$ kcal/mol), where S_A is the solvent-accessible surface area (SASA) computed by Sanner's algorithm in the MSMS program (*61*). The solute entropic contributions to the free energies were approximated with normal mode calculations (*36*, *62*). We employed the following protocol, as described previously (*36*). First, seven structures at 200 ps intervals were selected from the last 1.5 ns in each trajectory; then, using a distance-dependent dielectric function ($\epsilon = 4r$, where r is the interatomic distance in angstroms) to mimic solvent effects, steepest descent and conjugate gradient minimizations, followed by Newton−Raphson minimizations, were carried out with no cutoff for all nonbonded interactions until the root-mean-square deviation of the elements in the gradient vector was less than 10^{-4} kcal mol^{-1} Å^{-1} for each structure. Finally, we chose the minimized structure with the smallest rmsd compared to the MD average structure for each adduct, to estimate the translational, rotational, and vibrational entropies at 300 K.

Distortion Free Energy Analysis. To assess the distortions induced by the adduct, we computed a distortion free energy relative to the unmodified B-DNA control for the 10*S* (+) and 10*R* (−) adducts in the CA*C sequence context, using the ensembles obtained from the MD simulations. For each snapshot of the BP-modified DNA structures selected at 10 ps intervals, we excised the modified BP and replaced it with a hydrogen atom that is bonded with N^6 of the adenine base. The bond length was adjusted to the value of the other N^6−H bond. The chemical structure of this DNA duplex is thus the same as that of the unmodified DNA control duplex in our simulations. We then applied the MM-PBSA method to compute a free energy for these distorted but now chemically unmodified DNA duplexes, as well as for the normal unmodified control. We compared these data with the corresponding values for the unmodified duplex to estimate a distortion free energy ($\Delta G^{distort}$) caused by the intercalation:

$$\Delta G^{distort} = \Delta E^{d}_{int} + \Delta E^{d}_{vdW} + \Delta E^{d}_{electrostatic} + \Delta G^{d}_{PB} + \Delta G^{d}_{nonpolar} \quad (1)$$

where

$$\Delta E^{d}_{int} = E_{int}(\text{distorted DNA}) - E_{int}(\text{unmodified control}) \quad (2)$$

and

$$\Delta E^{d}_{vdW} = E_{vdW}(\text{distorted DNA}) - E_{vdW}(\text{unmodified control}) \quad (3)$$

and so on for the other terms.

Nucleotide Excision Repair Assay. Methods for the nucleotide excision repair assay for the 10*S* (+) and 10*R* (−)-*trans-anti*-[BP]-N^6-dA adducts in both the CA*A and CA*C sequence contexts were described in detail previously (*39*). In summary, site specific 10*S* (+) and 10*R* (−)-*trans-anti*-[BP]-N^6-dA adducts in the 5′-CGGACA*AGAAG-3′ *N-ras* oligonucleotide or in the 5′-CTCTCA*CTTCC-3′ sequence were obtained by incorporating appropriate phosphoramidites into the automated DNA synthesizer technique (*63*−*65*). After DNA synthesis, the modified oligonucleotides were deprotected and purified by reverse phase HPLC (*65*). The identity of individual adducts was assessed after enzymatic degradation (*25*, *65*) and confirmed by negative ion mode electrospray mass spectrometry (*66*).

To obtain internally labeled DNA duplexes of 139−146 base pairs, the modified oligonucleotides or their unmodified controls (70 pmol) were 5′ end-labeled with [γ-^{32}P]ATP (7000 Ci/mmol; ICN Pharmaceuticals) and mixed with five other partially overlapping oligonucleotides (100 pmol) that were phosphorylated with cold ATP. The oligonucleotides were annealed and ligated in the presence of T4 DNA ligase (Life Technologies, Inc.), followed by electrophoretic purification of the full-length fragments as described previously (*67*, *68*).

Oligonucleotide excision reaction mixtures (*67*−*69*) contained (in 25 μL) 35 mM HEPES-KOH (pH 7.9), 60 mM KCl, 40 mM NaCl, 5.6 mM $MgCl_2$, 2 mM ATP, dATP, dCTP, dGTP, and TTP (80 μM each), 0.8 mM DTT, 0.4 mM EDTA, 3.4% (v/v) glycerol, 5 μg of BSA, 5 fmol (75 000 dpm) of radiolabeled DNA substrate, and 50 μg (in protein equivalents) of *HeLa* cell extract. After the indicated incubation times at 30 °C, reactions were stopped by the addition of SDS [0.3% (w/v)] and proteinase K (200 μg/mL; Boehringer Mannheim), followed by proteinase K digestion for 15 min at 37 °C. DNA was purified by phenol/chloroform extraction and resolved by electrophoresis in 10% polyacrylamide denaturing gels, after which the radiolabeled excision products were visualized by autoradiography. The relative levels of excision were determined by densitometric analysis of oligonucleotides in the 24- to 32-mer size range on appropriately exposed X-ray films (using a Molecular Dynamics computing densitometer with ImageQuant software). The linearity of each densitometric quantification was confirmed by counting Cerenkov radiations of the corresponding gel slices.

RESULTS

Structural Analyses: Stable anti and syn Glycosidic Conformers in the 10S (+) Adduct. Two different starting models were employed in the 10*S* (+) adduct simulation, one with the orientation of the glycosidic torsion angle χ of −71.8°, in the overall *anti* region, and a second with this torsion at 21.1° in the *syn* region (see Materials and Methods). We used two starting models to carefully explore the conformational possibilities for χ, since experimental NMR investigations for this adduct with T opposite the lesion could not resolve the structures due to conformational heterogeneity, and a *syn*−*anti* equilibrium has been suggested as an important element in the mobility (*30*, *31*, *33*, *70*). Consequently, our starting models for this adduct had to be taken from NMR solution structures for the major *syn* conformer (*31*) and the minor conformer termed *anti* (*30*), which were sufficiently stabilized to be able to be resolved by NMR when mismatched with G. Interestingly, the starting model termed *anti* in this case [−71.8° as in the NMR model (*30*)] was not in the normal *anti* domain as found in B-DNA [$\chi \approx -110°$ to −140° (*71*)], but in an area known as a high-*anti* region (*72*).

In the case of the 10*R* (−) adduct, the experimental NMR studies indicate that such conformational heterogeneity plays only a very minor role (*32*−*34*). A normal *anti* conformation has been fully characterized by high-resolution NMR investigations and is very predominant (*34*). Consequently, we employed only this *anti* conformation ($\chi = -136.1°$), based on an NMR solution structure (*34*), as a starting model.

We monitored the time dependence of χ for each simulation and compared these with the unmodified control. Results are shown in Figure 2A. In the case of the unmodified control (green curve) and the 10*R* (−) adduct (blue curve), χ remained stably in the normal B-DNA *anti* range. For the 10*S* (+) adduct, the simulation initiated in the *syn* domain (orange curve) remained in that region and was quite stable after ∼200 ps. However, the simulation begun in the high-*anti* region (red curve) did not remain there stably throughout the 2.5 ns simulation. Instead, we see a high-*anti* region until ∼500 ps, a transitional region from ∼500 to 1000 ps, and then a stable normal *anti* domain until the end of the simulation (Figure 2A). As shown in Figure 2C, a structural transition at ∼500 ps in the 10*S* (+) isomer *anti* simulation is also revealed from the time dependence of the α' and β' torsion angles (Figure 1) that govern the orientation of the BP moiety with respect to the base. No such transition was observed for the other simulations. Furthermore, the time dependence of the pseudorotation phase angle *P* at A*6 also shows a transition, at ∼800 ps, from the C2′-*endo* to the C3′-*endo* domain, only in the 10*S* (+) *anti* simulation (Figure 2B).

Watson−Crick hydrogen bond analysis also supports the observed transition in the 10*S* (+) adduct *anti* simulation. Specifically, one of the two Watson−Crick hydrogen bonds between A*6 and T17, namely, N3−H3 (T17) to N1 (A*6), is ruptured prior to ∼500 ps and then forms and remains stably intact for the rest of the simulation, as shown in Figure S2 of the Supporting Information. In the *syn* simulation for this adduct, no Watson−Crick hydrogen bonds are present at any time. Moreover, no other types of hydrogen bonds between A*6 and T17 are observed in this case. In the 10*R* (−) adduct simulation, all Watson−Crick base pairs remain intact for this normal *anti* structure.

We monitored our simulations for possible formation of hydrogen bonds between hydroxyl groups on the BP moiety benzylic ring (Figure 1B) and DNA residues and did find that such hydrogen bonds formed in the 10*S* (+) adduct simulations. In the *anti* simulation, a hydrogen bond between N^4−H4 (C7) and O9 (BP) began to form after 500 ps and then remained stably in place until the end of the simulation (Figure 3C, red curve), with an occupancy of ∼85% in the 1−2.5 ns time frame. The *syn* simulation for this adduct also revealed a hydrogen bond involving the BP and the DNA, between O9−HO9 (BP) and O6 (G16) (occupancy of ∼78% over the 1−2.5 ns time frame) which did not, however,

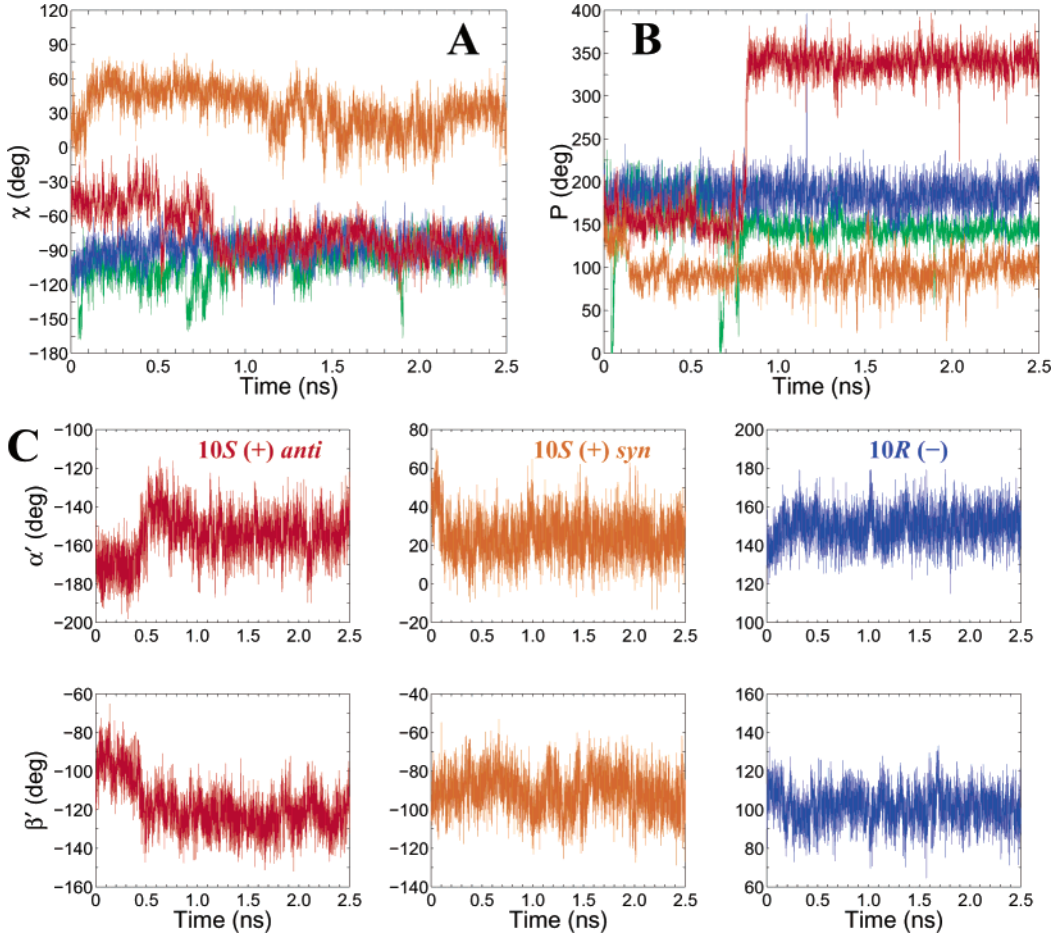

FIGURE 2: (A) Glycosidic torsion angle χ and (B) pseudorotation phase angle P in the modified adenine A*6 of the 10*S* (+) adduct *anti* and *syn* conformers, in the 10*R* (−) adduct, and in A6 of the unmodified control structure. (C) Torsion angles α' and β' for the 10*S* (+) adduct *anti* and *syn* conformers and the 10*R* (−) adduct. MD average χ values are −84.9 ± 12.4° for the 10*S* (+) adduct *anti* conformer (1−2.5 ns), −45.4 ± 12.9° for the 10*S* (+) adduct high-*anti* conformer (0−0.5 ns), 25.8 ± 17.3° for the 10*S* (+) adduct *syn* conformer (1−2.5 ns), −87.1 ± 12.0° for the 10*R* (−) adduct (1−2.5 ns), and −93.8 ± 12.5° for the unmodified control (1−2.5 ns). Average α' and β' torsion angle values are −154.4 ± 9.8° and −123.4 ± 9.0°, respectively, for the 10*S* (+) adduct *anti* conformer, 24.8 ± 10.2° and −91.8 ± 10.9°, respectively, for the 10*S* adduct (+) *syn* conformer, 150.7 ± 8.6° and 101.1 ± 9.0°, respectively, for the 10*R* (−) adduct (1−2.5 ns), and −168.6 ± 10.3° and −100.6 ± 11.9°, respectively, for the 10*S* (+) adduct high-*anti* conformer (0−0.5 ns). The color code is as follows: red, 10*S* (+) adduct *anti* conformer; orange, 10*S* (+) adduct *syn* conformer; blue, 10*R* (−) adduct; and green, unmodified control structure. Note that 0 ns is actually following the equilibration protocol described in Materials and Methods.

involve a transition (Figure 3C, orange curve). In the 10*R* (−) adduct simulation, no BP−DNA hydrogen bonds were observed that were maintained for any length of time.

Trajectory average helicoidal and backbone parameters are given in Figures S3 and S4 of the Supporting Information. These revealed the usual distortions needed to accommodate the intercalation of the planar and extended aromatic ring system in the 10*S* (+) and 10*R* (−) isomers (*36*). These torsional disturbances in and near the intercalation pocket, which produce the stretching and unwinding needed for insertion of the aromatic moiety between the base planes, are similar in the CA*A and CA*C sequences (Figures S3 and S4 of the Supporting Information). Specifically, rise adopts average values of 8.0 and 8.3 Å at the intercalation pocket in the 10*S* (+) (*anti* glycosidic conformer[2]) and 10*R* (−) isomers (Table S2 of the Supporting Information), respectively, compared to the normal values of 3.7 and 3.3 Å, respectively, in the same base pair step for the unmodified control. Buckle and propeller at the modified base pair are also deviated, oppositely as expected (*36*), in the 10*S* (+) (*anti* glycosidic conformer) and 10*R* (−) adducts (Figure S3). Similar local unwinding due to the intercalation of BP is also found in both adducts (Table S2). The quality of Watson−Crick hydrogen bonding in the *anti* conformers is similar in the two sequence contexts (Table S2). A notable distinction in the case of the CA*C sequence 10*S* (+) adduct *anti* conformer, however, is the roll value. The trajectory average roll is 30° for the 10*S* (+) adduct *anti* conformer, while it is 4° for the 10*R* (−) adduct (Table S2). Since high roll values are associated with DNA bending (*75*), we monitored DNA bending in our simulations (Figure S5 of the Supporting Information). We first note that the trajectory-averaged bend angle for the unmodified control is 21.1 ± 9.9° over the 1−2.5 ns time frame and 20.3 ± 9.3° over the first nanosecond. However, the 10*S* (+) adduct *anti* simulation showed average bend angles of 43.8 ± 12.4° over the 0−0.5 ns time frame and 60.1 ± 9.8° over the 1−2.5 ns time frame. By contrast, the *syn* simulation for this adduct gave a trajectory-averaged bend angle of 24.5 ± 12.1° over the 1−2.5 ns time frame (19.6 ± 11.7° over the 0−1 ns

[2] *syn* conformers are not amenable to reliable helical parameter calculations which depend on Watson−Crick base pairing (*73*, *74*).

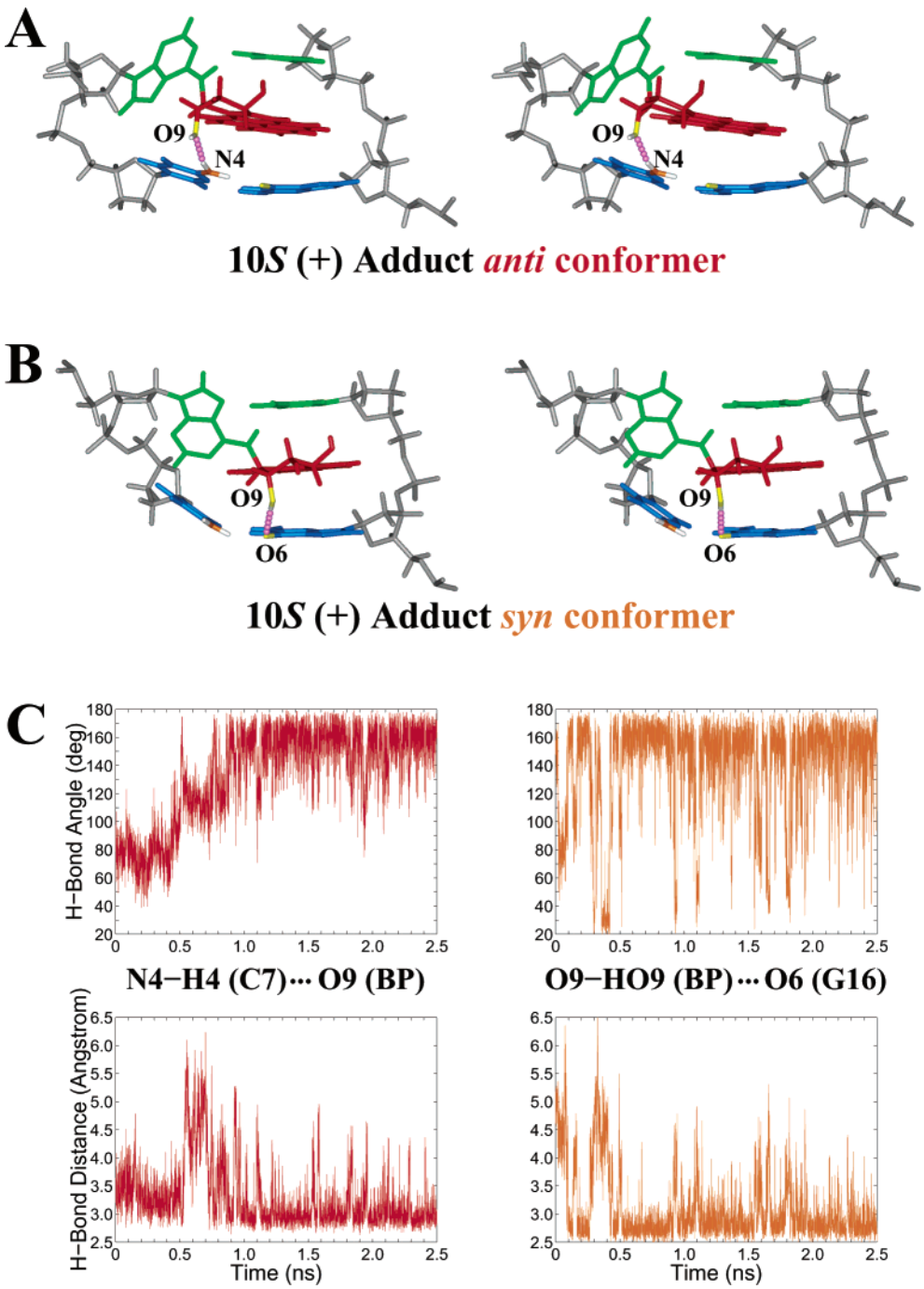

FIGURE 3: Stereoviews of the (A) *anti* and (B) *syn* conformations of the 10*S* (+) adduct [d(A*C)·d(GT)]. BP is in red, the A*6−T17 pair in green, and the C7−G16 pair in blue. The backbone and sugar atoms are in gray. O9 on BP and O6 on G16 are in yellow, and N^4 on C7 is in orange; the hydrogen atoms of the O9−HO9 hydroxyl group on BP and the N^4 amino group on C7 are in white. The hydrogen bonds between N^4−H4 (C7) and O9 (BP) in the *anti* conformer and between O9−HO9 (BP) and O6 (G16) in the *syn* conformer are shown as solid pink dots. All stereoimages are constructed for viewing with a stereoviewer. (C) Time dependence of the hydrogen bond angle and distance for the sequence-dependent hydrogen bonds between N^4−H4 (C7) and O9 (BP) (*anti* conformer) and between O9−HO9 (BP) and O6 (G16) (*syn* conformer) of the 10*S* (+) adduct in the CA*C sequence context over the 2.5 ns MD simulation.

time frame). For the 10*R* (−) adduct, trajectory-averaged bend angles are 18.1 ± 8.7° over the first nanosecond and 21.9 ± 9.4° from 1 to 2.5 ns. Thus, significant bending compared to the unmodified control is found only in the 10*S* (+) adduct *anti* simulation. Figure 4 shows the average 10*S* (+) (*anti* and *syn* glycosidic conformers) and 10*R* (−) adduct structures, as well as the unmodified control structure, derived from our simulations.

Thermodynamic Analyses: Similar Stabilities of anti and syn Glycosidic Conformers in the 10S (+) Adduct. The free energy analyses showed that the *anti* and *syn* glycosidic structures of the 10*S* (+) adduct have similar total free energies, while both are more stable than the initial high-*anti* structure of this adduct. Specifically, as shown in Table 1, the total free energy difference between the *anti* and *syn* structures of the 10*S* (+) adduct is negligible, only 1.3 kcal/mol favoring the *syn* structure; however, the high-*anti* initial structure of the 10*S* (+) adduct has a much higher energy than the *anti* and *syn* structures, by 12.2 and 13.5 kcal/mol, respectively. Evidently, this starting model, taken out of

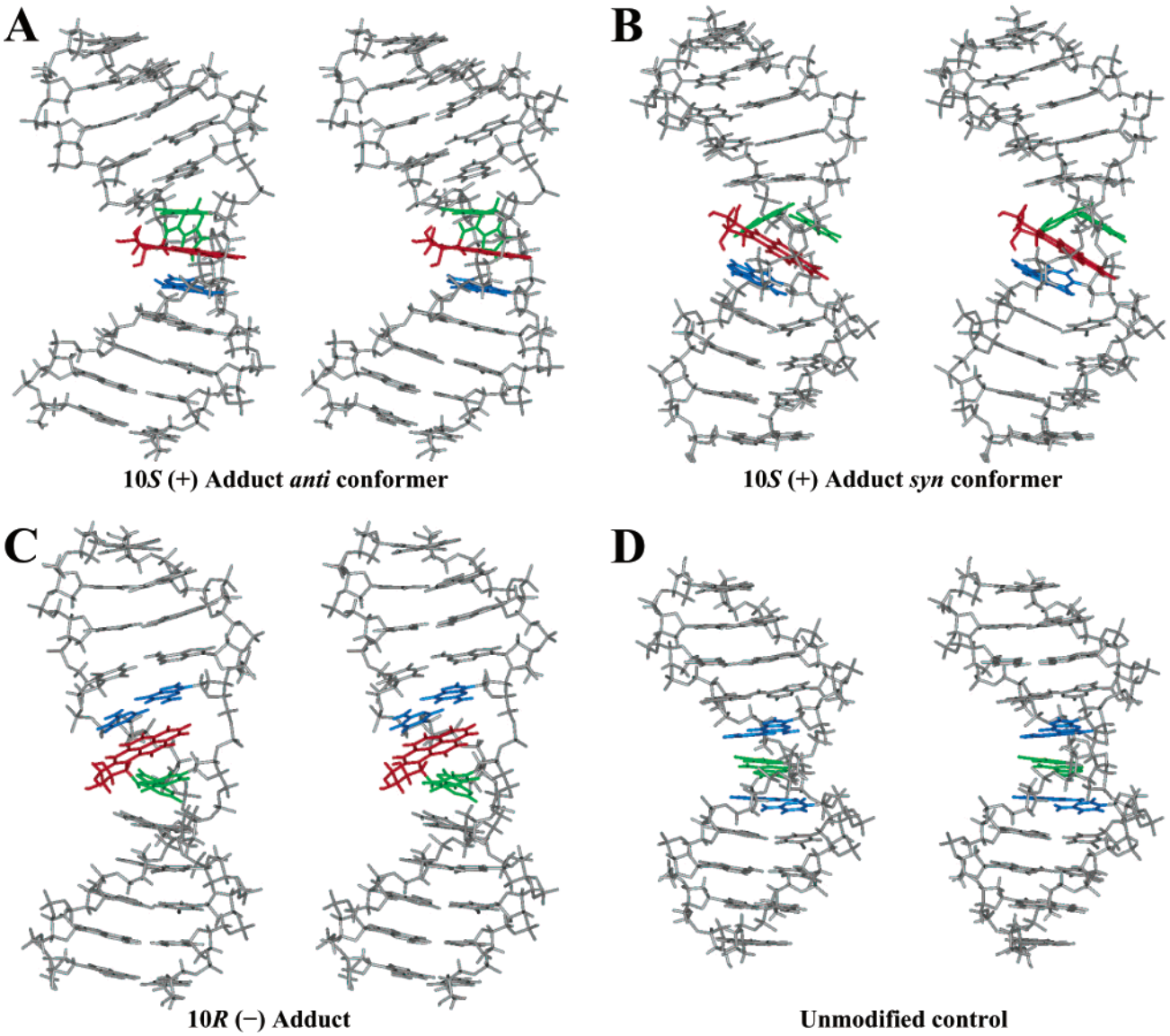

FIGURE 4: Stereoviews of the MD average structures over 1−2.5 ns. (A) 10*S* (+) adduct *anti* conformer and (B) *syn* conformer with BP in red, the A*6−T17 pair in green, and the C7−G16 pair in blue. (C) 10*R* (−) adduct with BP in red, the C5−G18 pair in blue, and the A*6−T17 pair in green. (D) Unmodified control B-DNA structure with the C5−G18 and C7−G16 pairs in blue and the A6−T17 pair in green. The backbone and sugar atoms and other residues are in gray. All structures are aligned so that the 5′-OH groups are at the top left.

Table 1: Free Energy Component Analysis of the 10*S* (+)- and 10*R* (−)-*trans*-*anti*-[BP]-N^6-dA DNA Adducts in the CA*C Sequence Context[a]

	10*S* (+) *anti*	10*S* (+) *syn*	10*S* (+) high-*anti*	10*R* (−)	Δ_1	Δ_2
$\langle E_{electrostatic} \rangle$	265.0 (38.9)	350.9 (48.3)	339.7 (36.3)	330.7 (57.8)	−65.7	20.2
$\langle E_{vdW} \rangle$	−184.8 (9.1)	−184.6 (9.3)	−187.5 (10.9)	−183.7 (9.5)	−1.1	−0.9
$\langle E_{int} \rangle$	1007.1 (18.9)	1000.5 (16.3)	1009.3 (17.9)	996.3 (17.3)	10.8	4.2
$\langle E_{MM} \rangle$	1087.3 (36.9)	1166.8 (46.4)	1161.5 (36.4)	1143.2 (61.5)	−55.9	23.6
$\langle G_{nonpolar} \rangle$	25.4 (0.2)	25.0 (0.2)	25.4 (0.1)	25.3 (0.2)	0.1	−0.3
$\langle G_{PB} \rangle$	−5553.0 (35.3)	−5630.7 (44.2)	−5616.0 (31.0)	−5620.8 (56.5)	67.8	−9.9
$\langle G_{solvation} \rangle$	−5527.7 (35.4)	−5605.8 (44.4)	−5590.6 (31.0)	5595.5 (56.5)	67.8	−10.3
$\langle G_{PB} + E_{electrostatic} \rangle$	−5288.0 (10.9)	5279.9 (10.7)	−5276.2 (13.7)	−5290.1 (11.8)	2.1	10.2
$\langle E_{MM} + G_{PB} \rangle$	−4465.7 (16.0)	−4463.9 (14.3)	−4454.5 (14.2)	−4477.6 (14.9)	11.9	13.7
$-TS$	−591.0	−593.7	−590.0	−592.3	1.3	−1.4
G_{tot}	−5031.3	−5032.6	−5019.1	−5044.6	13.3	12.0

[a] All energies are in kcal/mol. Values in parentheses are standard deviations. Δ_1 = 10*S* (+) *anti* − 10*R* (−), and Δ_2 = 10*S* (+) *syn* − 10*R* (−).

necessity from a G−A* mismatch structure because no other suitable one was available, is not stable when the normal partner T is opposite the lesion. The enthalpic contribution to the free energy favors the 10*R* (−) adduct by 11.9 and 9.4 kcal/mol, relative to the *anti* and *syn* conformers of the 10*S* (+) adduct, respectively, largely due to the internal (E_{int}) and electrostatic free energy ($G_{PB} + E_{electrostatic}$) differences. Melting data in this sequence context (*76*) for the 11-mer 10*S* (+) (25 °C) and 10*R* (−) (32 °C) adducts also reveal greater thermal stability for the 10*R* (−) adduct. The solute entropic term is greatest for the *syn* structure of the 10*S* (+) adduct compared to all the other structures, probably because

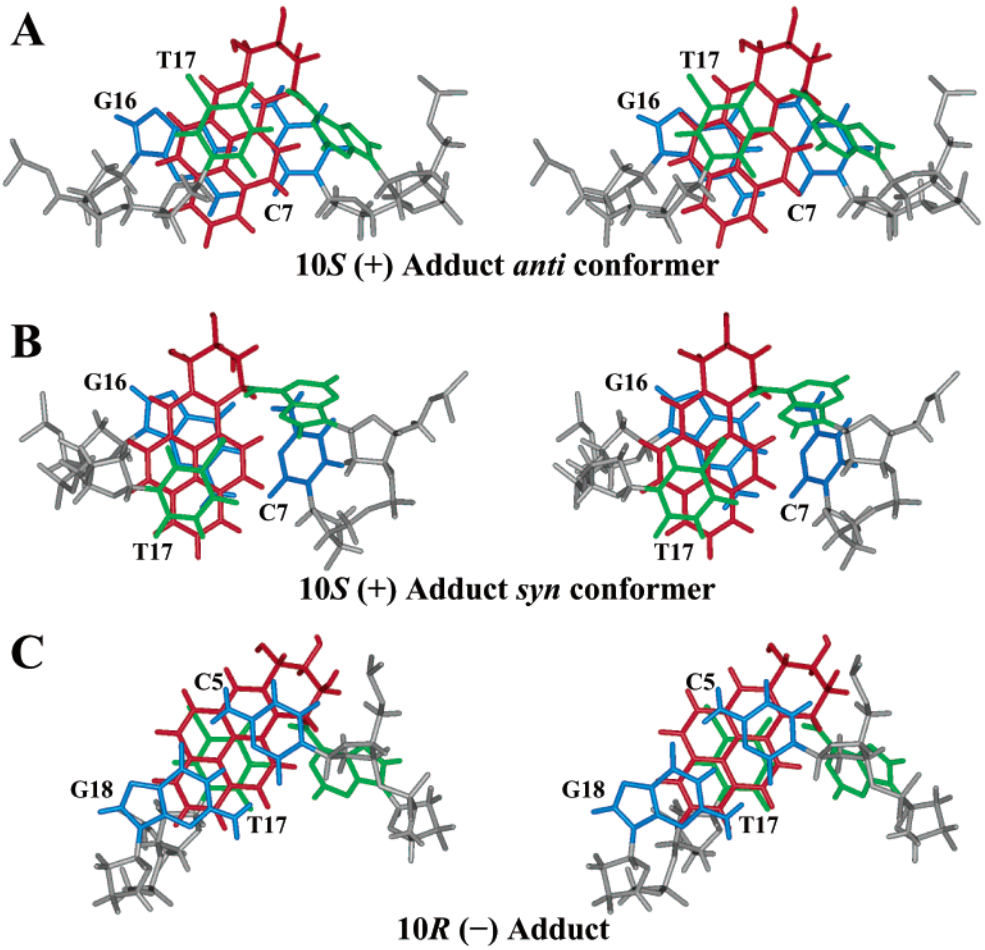

FIGURE 5: Stereoviews of the intercalation pockets of the 10*S* (+) [d(A*C)·d(GT)] and 10*R* (−) [d(CA*)·d(TG)] adducts. In the (A) *anti* conformer and (B) *syn* conformer of the 10*S* (+) adduct, BP is shown as a red stick, the A*6−T17 pair as a green stick, and the C7−G16 pair as a blue stick. (C) In the 10*R* (−) adduct, BP is shown as a red stick, the A*6−T17 pair as a green stick, and the C5−G18 pair as a blue stick. All backbone and sugar atoms are in gray. The view is along the helix axis from 5′ to 3′ along the modified strand.

Table 2: van der Waals Interaction Energies at the Intercalation Pocket[a]

	10*S* (+) *anti*	10*S* (+) *syn*	10*R* (−)
BP−T17	−13.0	−11.5	−12.3
BP−C7/C5	−6.2	−5.9	−10.5
BP−G16/G18	−10.5	−13.2	−8.0
total	−29.7	−29.6	−30.8

[a] BP−C7 and BP−C5 are for 10*S* (+) and 10*R* (−) adducts, respectively. BP−G16 and BP−G18 are for 10*S* (+) and 10*R* (−) adducts, respectively. All energies are in kcal/mol.

of greater flexibility due to lack of Watson−Crick base pairing at the lesion site.

We evaluated a distortion free energy due to adduct intercalation for our simulated structures (see Materials and Methods). As shown in Table S1 of the Supporting Information, the total distortion free energy $\Delta G^{distort}$ is 21.8 and 25.4 kcal/mol for the 10*S* (+) adduct *anti* and *syn* conformers, respectively, and 13.9 kcal/mol for the 10*R* (−) adduct.

In addition, we computed the energies for van der Waals interaction between BP and the residues involved in the intercalation pocket in the 10*S* (+) (both *anti* and *syn* conformers) and 10*R* (−) adducts, and found that these exhibit similar values (Table 2). These results are in accord with structural observations. Specifically, the overlap between the BP aromatic moiety and the adjacent base pairs is quite similar in the 10*S* (+) (both *anti* and *syn* conformers) and 10*R* (−) adducts. The aromatic rings of BP in the 10*S* (+) adduct *anti* and *syn* structures stack with the partner T17 of the modified nucleotide A*6 quite well; furthermore, the BP aromatic rings have substantial overlap with the adjacent G16, but they do not stack with the adjacent C7 base (Figure 5A,B). In the 10*R* (−) adduct, the BP aromatic rings also stack well with the normal partner T17 of the adducted adenine residue A*6 (Figure 5C). However, the BP aromatic rings in the 10*R* (−) adduct have less overlap with the adjacent G18, compared to the overlap with G16 in the case of the 10*S* (+) adduct; however, the BP rings stack better with C5 in the 10*R* (−) adduct than with C7 in the 10*S* (+) adduct (Figure 5).

Relative Nucleotide Excision Repair Activities. Linear and internally γ-^{32}P-labeled DNA fragments containing a site specific adduct were incubated in a defined *HeLa* cell extract that had been shown to contain the entire repertoire of core NER factors (*67*−*69*). After 40 min at 30 °C, the reaction mixtures were separated by denaturing polyacrylamide gel electrophoresis to visualize the specific excision products consisting of oligonucleotides in the size range of 24−32 residues. A quantitative evaluation was performed after autoradiography of the dried gel and laser scanning densitometry of the bands representing excision products and the full-length substrate in each lane. The excision activities were

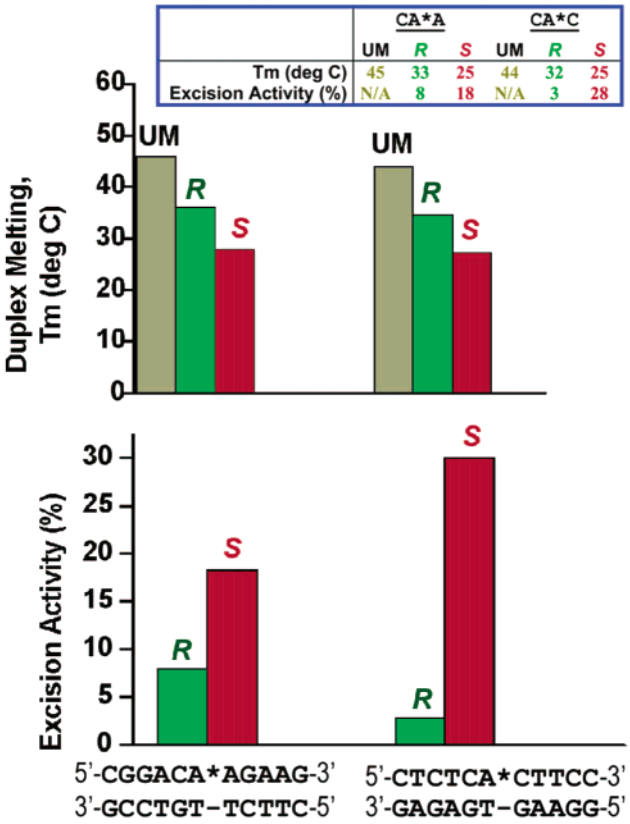

FIGURE 6: Relative nucleotide excision repair activities and duplex melting temperatures for the 10*S* (+)- and 10*R* (−)-*trans*-*anti*-[BP]-N^6-dA adducts in the CA*A (*39*) and CA*C sequence contexts. The melting temperatures for the unmodified controls are shown in gray.

compared to a standard substrate containing a 10*S* (−)-*cis*-*anti*-[BP]-N^2-dG adduct (*39*). The relative yields of excision products were in the linear, initial kinetic region. Examples of such kinetic curves have been published previously (*39*). We found that both the 10*S* (+)- and 10*R* (−)-*trans*-*anti*-[BP]-N^6-dA adducts in the CA*A (*39*) and current CA*C sequence contexts were processed by NER enzymes in *HeLa* cell extracts. Quantitative analysis of specific excision products in the 24−32-nucleotide range showed that the relative NER activities for the 10*S* (+)- and 10*R* (−)-*trans*-*anti*-[BP]-N^6-dA adducts in the CA*A context are ∼18 and ∼8%, respectively, while they are ∼28 and ∼3%, respectively, in the current CA*C context. The relative NER activities and the melting temperatures, T_m, for the 10*S* (+) and 10*R* (−) adducts in the CA*A and CA*C sequences are shown in Figure 6. The data show that the *S* isomers are repaired more than the *R* isomers, independent of sequence, and in the case of the 10*S* (+) adduct, the CA*C sequence is more repaired than the CA*A sequence. Furthermore, the thermal melting data indicate that the more repaired adducts have lower thermal melting temperatures relative to the unmodified duplexes than their less repaired counterparts.

DISCUSSION

Influence of Base Sequence Context on Conformational Equilibria

syn−*anti Equilibrium.* One goal of this study was to elucidate the influence of base sequence context on conformational equilibria in a system which had not been amenable to full molecular characterization through experimental NMR investigations due to conformational heterogeneity. Hence, simulation studies could play a useful role. In particular, we are interested in the 10*S* (+)-*trans*-*anti*-[BP]-N^6-dA adduct in a DNA duplex opposite its normal partner T, comparing its conformational properties in the CA*C sequence context examined here with those deduced previously in the CA*A sequence context (*36*). We also examined the corresponding 10*R* (−)-*trans*-*anti*-[BP]-N^6-dA adduct whose NMR solution structure has been determined in a number of sequence contexts (*33*, *34*), since conformational heterogeneity is much lower in this isomer.

Our studies involved 2.5 ns molecular dynamics simulations, in which all starting structures and protocols were identical for the present CA*C investigation to those employed previously for the CA*A work (*36*). Yet, we noted a remarkable difference in the two trajectories. In the CA*C case, a conformational transition was observed in the 500−1000 ps time frame, from the starting structure in which the glycosidic torsion angle was high-*anti* to the normal B-DNA *anti* domain (Figure 2A). This transition was accompanied by a number of additional conformational rearrangements: a shift in the α′ and β′ carcinogen−base linkage torsion angles, the formation of the N3−H3 (T17) to N1 (A*6) Watson−Crick hydrogen bond which had been ruptured, a transition in the sugar pucker from the C2′-*endo* to the C3′-*endo* region at A*6 (Figure 2B), and the formation of a hydrogen bond between N^4−H4 (C7) and O9 (BP) (Figure 3C). Following the transition, the simulation showed stability until the end. Our free energy analysis showed that the initial, high-*anti* state was ∼12.2 kcal/mol higher in energy than the stable *anti* form. By contrast, our earlier simulation in the CA*A sequence context for the same 10*S* (+) isomer showed no such transition (*36*). Instead, the glycosidic torsion angle χ visited the entire *anti*/high-*anti*/*syn* region (Figure 7). Thus, these results suggest an energy surface for the glycosidic torsion angle χ with three wells, *anti*, high-*anti*, and *syn*, in accord with well-known preferences for nucleic acids (*77*−*81*). It is noteworthy that the high-*anti* domain has been particularly observed (*82*, *83*) and noted through computational studies for intercalation complexes (*84*). Furthermore, the energy landscape is modulated by the different sequence contexts. In the CA*A case, the energy well centered at high-*anti* appears to be broad with little barrier to either the *anti* or the *syn* domain, offering easy access to these regions (Figure 7, black curve). On the other hand, in the CA*C sequence, a *syn* and an *anti* well with little accessibility between them is suggested, indicating a higher barrier (Figure 7, red and orange curves).

Because the *syn* domain was not sampled through our CA*C simulation starting from the high-*anti* region, we carried out an additional simulation that began with the glycosidic torsion angle *syn* (Figure 2A, orange curve). This simulation showed a stable *syn* glycosidic conformation whose free energy was very similar to that of the normal *anti* glycosidic conformer (Table 1) which had become stable after 1 ns during the simulation that began at high-*anti*. Thus, our simulations suggest that a *syn* conformer contributes significantly to the conformational heterogeneity in both sequence contexts, but that the barrier between *syn* and *anti* domains is greater in the CA*C case, as the simulation was

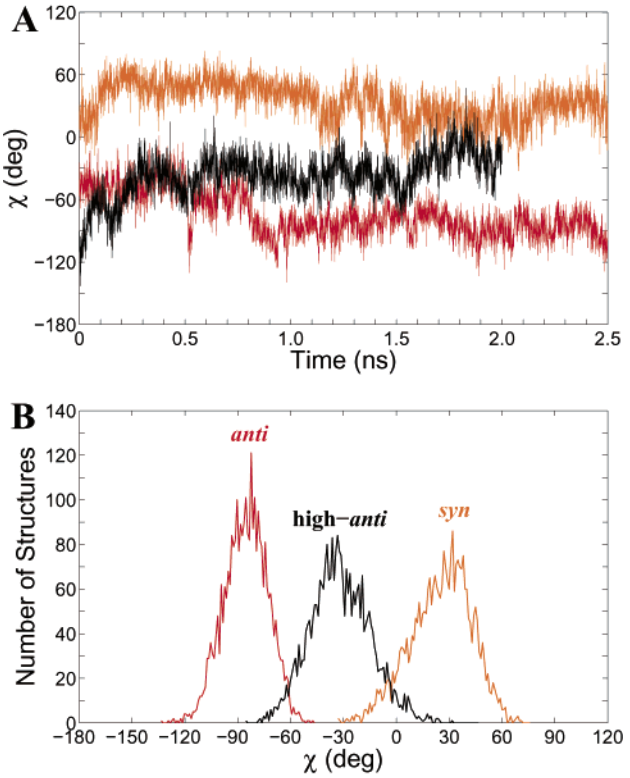

FIGURE 7: (A) Time dependence and (B) distribution of the glycosidic torsion angle χ at A*6 in the CA*A (*36*) and CA*C sequence contexts. The color code is as follows: black, 10*S* (+) adduct in the CA*A sequence (*36*); red, 10*S* (+) adduct *anti* conformer in the CA*C sequence; and orange, 10*S* (+) adduct *syn* conformer in the CA*C sequence. Our earlier simulation for the CA*A sequence (black) (*36*) was carried out for only 2 ns. The curves correspond well to the *anti*, high-*anti*, and *syn* domains that have been found for nucleic acid structures both experimentally and computationally (*77*−*84*).

unable to sample the *syn* state from the high-*anti* starting structure in this case only. This barrier appears to stem from the hydrogen bonds involving the O9−HO9 hydroxyl group on the BP benzylic ring and the adjacent bases in both the *anti* and *syn* conformations, namely, N^4−H4 (C7) to O9 (BP) in the *anti* conformer and O9−HO9 (BP) to O6 (G16) in the *syn* conformer (Figure 3A,B), which likely stabilize both the *anti* and *syn* conformations in the CA*C sequence. Possibly, the high-energy high-*anti* conformation is near a transition state between the stable normal *anti* and *syn* conformations in the CA*C sequence context opposite T (Table 1).

Our simulation for the 10*R* (−) adduct was very similar in the present CA*C sequence as in the previous CA*A case, with stable *anti* conformations and no evidence for a *syn* component. Recent work (*33*) indicates that a minor *syn* conformer can be present for this isomer, at least in the AA*G sequence context. While our trajectory did not find a *syn* conformer, its possibility as a minor constituent remains open.

Sequence-Dependent Hydrogen Bond. We sought to determine why the simulation behaved so differently in the CA*A and CA*C sequences when all other variables (starting conformations and MD protocols) were identical. The key seems to lie in the hydrogen bond between O9 (BP) and N^4−H4 (C7) that forms during the transition from the high-*anti* to the normal *anti* conformation and then remains in place during the rest of the simulation. This hydrogen bond is sequence-dependent. Since it is between O9 on the BP benzylic ring and the amino group on the 3′-side neighboring cytosine C7, it can only be formed in the CA*C sequence. In the CA*A sequence, this cytosine is replaced with an adenine which cannot, when normally positioned in B-DNA, contribute a hydrogen bond donor to O9 of BP. Moreover, as mentioned in the Results, the 10*S* (+) adduct *syn* glycosidic conformer in the CA*C sequence also has a hydrogen bond involving BP and DNA, between O9−HO9 (BP) and O6 (G16) (Figure 3B). However, as noted by a reviewer, an analogous hydrogen bond should be feasible in the CA*A sequence, involving N^6 of A7 and O9−HO9 (BP). Accordingly, we re-examined our CA*A simulation data and did find that a very weak hydrogen bond/electrostatic interaction involving N^6 (A7) and O9−HO9 (BP) can occur when the *syn* domain for the glycosidic torsion angle is traversed (Figure S6 of the Supporting Information).

Interestingly, Pradhan et al. have obtained a high-resolution NMR solution structure of a 10*S* (+) adenine adduct derived from (+)-*syn*-BPDE [(+)-(7*S*,8*R*,9*S*,10*R*)-7,8-dihydroxy-9,-10-epoxy-7,8,9,10-tetrahydrobenzo[*a*]pyrene] via *trans* epoxide opening, also in the CA*C sequence context (*70*). They proposed that a hydrogen bond between O7−HO7 (BP) and N7 of G16 stabilizes their major (*syn* glycosidic torsion) conformer or slows its rate of interconversion, which effectively means raising the barrier (*70*). Moreover, ROESY experiments provided evidence for interconversion between the major, *syn* and a minor, possibly *anti* glycosidic conformer (*70*). Since the orientation of O9 on the benzylic ring is the same for both the 10*S* (+)-*trans*-*anti*-[BP]-N^6-dA and the 10*S* (+)-*trans*-*syn*-[BP]-N^6-dA adducts (Chart 1), it is conceivable that the hydrogen bond between O9 (BP) and N^4−H4 (C7) found in our simulation, which stabilizes the *anti* glycosidic conformer derived from *anti*-BPDE, may also contribute to the stability of the minor, possibly *anti* glycosidic conformer derived from *syn*-BPDE.

Thus, our simulations are in harmony with the broad spectrum of experimental data (*30*−*34*, *70*) that indicate a delicate *syn*−*anti* glycosidic bond equilibrium for a 10*S* (+) adduct, whose population balance can be easily affected by the nature of the partner base, the stereochemistry of the benzylic ring, and the neighboring base sequence context, with the possibility of sequence- or stereochemistry-dependent hydrogen bonds involving the BP and neighboring bases playing a significant role.

Chart 1

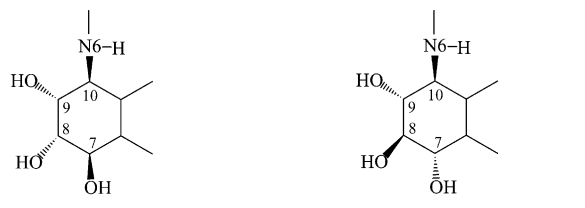

Benzylic Ring of 10*S* (+)-*trans*-*anti*-[BP]-N^6-dA

Benzylic Ring of 10*S* (+)-*trans*-*syn*-[BP]-N^6-dA

DNA Roll and Bending. The very easily perturbed *syn*−*anti* conformational equilibrium may play a role in elucidating DNA bending effects in the 10*S* (+) adenine adduct. Our simulations revealed one helical parameter that was

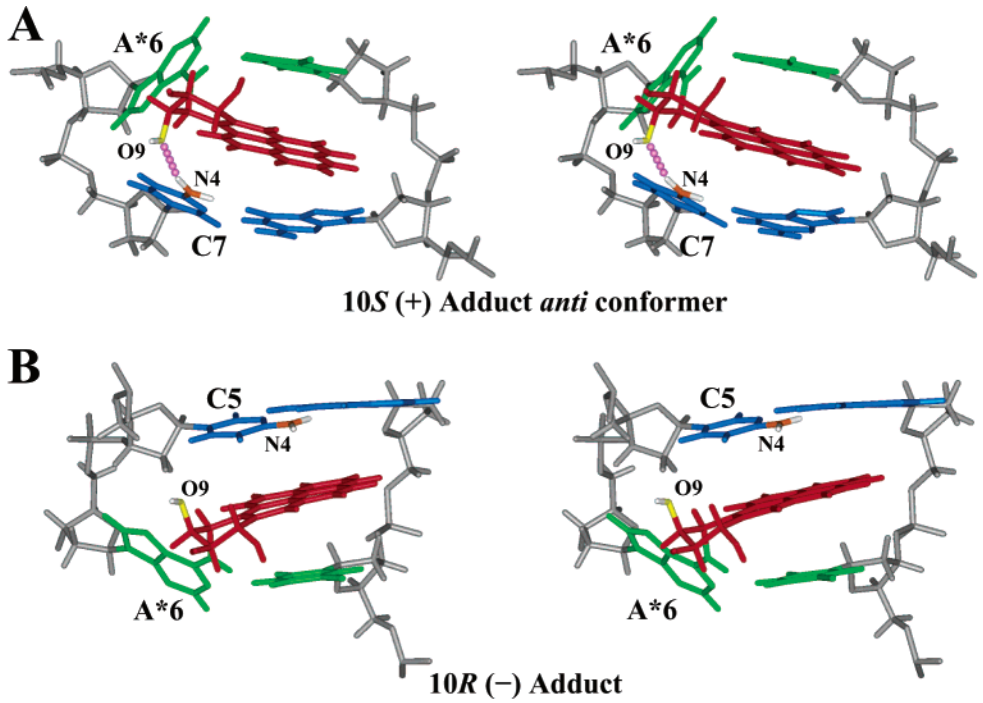

FIGURE 8: Stereoviews of the intercalation pockets of the (A) 10*S* (+) adduct *anti* conformer [d(A*C)·d(GT)] and (B) 10*R* (−) adduct [d(CA*)·d(TG)]. BP is in red, the A*6−T17 pair in green, the C7−G16 pair in blue, and the C5−G18 pair in blue. O9 on BP is in yellow, and N^4 on C5 and C7 is in orange; the hydrogen atoms of the O9−HO9 hydroxyl group on BP and the N^4 amino group on C5 and C7 are in white. The hydrogen bond between N^4−H4 (C7) and O9 (BP) is shown as solid pink dots. The backbone and sugar atoms are in gray.

distinctly different in the CA*C sequence compared to the CA*A sequence in the 10*S* (+) isomer, namely, the value of roll. Roll is known to be the primary helical parameter that governs DNA bending (*75*). Our simulations indicate essentially no significant additional roll or bending above the unmodified control in the CA*A sequence or the *syn* glycosidic conformer in the CA*C sequence; however, we do find a significant bend, correlated with the sequence specific hydrogen bond, N^4−H4 (C7) to O9 (BP), only in the *anti* conformer of the CA*C sequence. As shown in Figure 3, a hydrogen bond between O9 (BP) and N^4−H4 (C7) occurs in the structure of the *anti* conformer over 1−2.5 ns; however, it is not present in the starting high-*anti* conformer over 0−0.5 ns or during the transition over the 0.5−1 ns time frame. The formation of this N^4−H4 (C7)···O9 (BP) hydrogen bond is accompanied by additional DNA bending in the 10*S* (+) adduct (Figure S5), suggesting that this hydrogen bond may help stabilize the bent *anti* conformation. However, such a bend could be very easily perturbed via destabilization of the hydrogen bond with concomitant rebalancing of the *syn*−*anti* equilibrium. Experimental bending studies through gel mobility and ligation investigations may have unknown effects on this equilibrium. Experimental results for this isomer in the CA*A sequence context (*85*) suggest little additional bending over the unmodified control, in line with our simulation for this sequence. Experimental results are similar for the CA*C sequence context (N. E. Geacintov laboratory, unpublished data); it is possible that experimental conditions might stabilize either the *syn* or the *anti* glycosidic conformer, and thus affect the observed bending in this sequence.

Another intriguing question is why the 10*S* (+) *anti* conformer is more bent than the 10*R* (−) adduct, even though the 3′-intercalated BP and the 5′-intercalated BP in the respective 10*S* (+) and 10*R* (−) adducts have the same neighboring base (cytosine) in the CA*C sequence context. Recall that the 10*S* (+) adduct is intercalated on the 3′-side of A*, while the 10*R* (−) adduct is 5′-intercalated. The hydrogen bond between N^4−H4 (C7) and O9 (BP) may play a role here also. Such a hydrogen bond is not feasible between the BP and the neighboring cytosine (C5) in the 10*R* (−) adduct in the CA*C sequence, because the right-handed helical twist of B-DNA precludes its formation. In the 10*S* (+) adduct (Figure 8A), the amino group of the 3′-side neighboring cytosine, C7, is twisted *toward* the O9−HO9 axial hydroxyl group on BP, placing the donor and acceptor atoms in proximity; however, in the 10*R* (−) adduct (Figure 8B), the free amino group of the 5′-side cytosine, C5, is twisted *away* from the O9−HO9 axial hydroxyl group of BP so that no stabilizing hydrogen bond can be formed.

Other Conformational Flexibilities: Sugar Pucker and External Conformers. The role that other conformational sources of flexibility play in the conformational heterogeneity of the 10*S* (+) adduct is also of interest. We do note that the *anti* conformer in our simulation adopts the C3′-*endo* sugar conformation in the CA*C sequence context, while the *syn* conformer has the A*6 sugar C2′-*endo* (Figure 2B). Zegar et al. (*32*) found a C3′-*endo*−C2′-*endo* sugar pucker interconversion at A, 5′ to the modified A*, for the 10*R* (−) adduct in the CAA* sequence. Interestingly, we found a similar C3′-*endo*−C2′-*endo* sugar pucker interconversion at the 5′-side neighboring base C5 for the 10*S* (+) adduct in the CA*C sequence (Figure S7 of the Supporting Information). Our simulations did not reveal any evidence for a conformational component in which the bulky carcinogen is placed in a position that is on the helix exterior, although experimental data (*33*) suggest that such a component may be contributing somewhat to the conformational mix in the 10*S* (+) adduct.

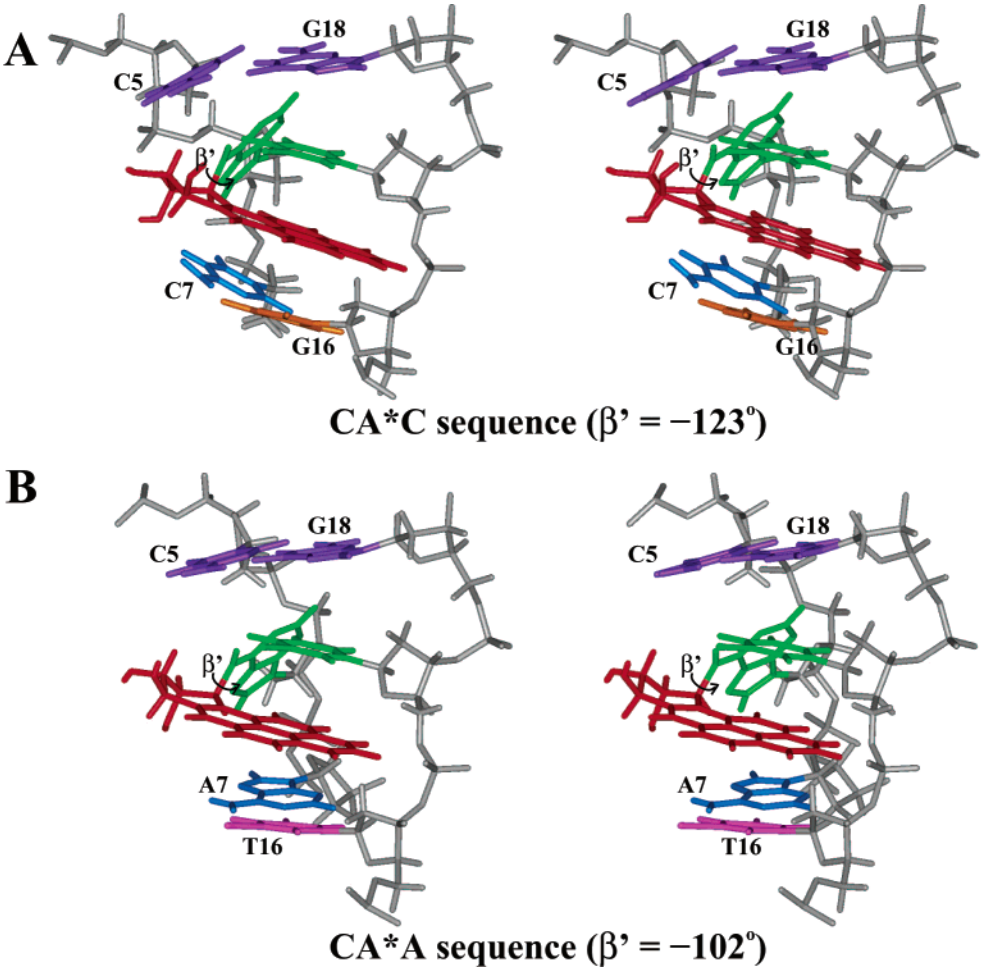

FIGURE 9: (A) Stereoview of the d(CA*C)·d(GTG) region of the 10*S* (+) adduct *anti* conformer in the CA*C sequence context. BP is in red, the A*6−T17 pair in green, the C5−G18 pair in violet, C7 in blue, and G16 in orange. (B) Stereoview of the d(CA*A)·d(TTG) region of the 10*S* (+) adduct in the CA*A sequence context. BP is in red, the A*6−T17 pair in green, the C5−G18 pair in violet, A7 in blue, and T16 in magenta. All backbone and sugar atoms are in gray.

Free Energy and the Steric Effect. As in the CA*A sequence, the free energy of the 10*R* (−) isomer is significantly lower than that of the 10*S* (+) isomer (*36*), in line with thermal melting data [10*S* (+) adduct, 25 °C; 10*R* (−) adduct, 33 °C] (*76*), which indicates less stability for the 10*S* (+) isomer. This lower stability stems essentially from a stereochemical effect of the BP benzylic ring system (Figure 1) which, in combination with the 3′-side intercalation of the BP ring system and the right-handed helical twist of the DNA, places the OH-containing benzylic ring system in a crowded position in the 10*S* (+) isomer (*30*, *33*, *36*). The *syn*−*anti* conformational equilibrium, local unwinding, and diminished stacking interactions between BP and the intercalation pocket all have a hand in causing the diminished stability, which results from the need to alleviate the crowding in this 10*S* (+) isomer only.

However, the dynamic balance between these various contributions appears to depend on sequence. Rotation of the glycosidic bond χ to the *syn* domain is utilized (*33*) in both sequences. In addition, unwinding plays a greater role in alleviating the steric crowding in the CA*A than in the CA*C sequence; we previously found total unwinding near the lesion site in the CA*A case of ∼41° (*36*), while in the CA*C sequence, *anti* conformation total unwinding near the lesion site is only ∼28° (Table S2). Instead, the crowding in the *anti* conformer is alleviated by rotating the linkage torsion angle β', which turns the benzylic ring of BP away from the sterically crowded region at C5 on its 5′-side (Figure 9, β' is −123° in the CA*C sequence and −102° in the CA*A case). This rotation of β' optimizes the overlap between the aromatic region of BP and the 3′-side neighboring G16 base (Figure 5A). However, in the CA*A sequence, the base is T16 with only one aromatic ring to stack with BP (*36*). This is consistent with the observation that the van der Waals interaction energy at the intercalation pocket of the 10*S* (+) adduct in the CA*C sequence context (−29.7 kcal/mol for the *anti* conformer) is greater than in the CA*A sequence context [−26.9 kcal/mol (*36*)], largely due to the increased number of interactions between BP and the 3′-side neighboring G16 base (Table 2). Thus, the base sequence context, specifically, the 3′-neighboring purine G16, plays the essential role in dictating the strategy to avoid crowding. In the CA*C sequence *anti* conformer, it involves rotation of β', while in the CA*A sequence, additional unwinding helps provide the needed space.

Structural Rationale for Sequence- and Stereoisomer-Dependent Nucleotide Excision Repair

Our combined structural and thermodynamic studies suggest a rationale for the observed sequence dependence in our NER assay. It is believed that the NER damage recognition machinery initially recognizes the distortions in

the normal DNA helical structures induced by lesions rather than recognizing the lesion per se (*86*−*88*). The disruption or weakening of Watson−Crick hydrogen bonding (*69*, *89*), DNA bending (*90*−*92*), and unwinding of the DNA double helix are considered to be such distortions recognized by the NER factors in a multipartite NER recognition model (*93*).

The NER results shown in Figure 6 reveal the sequence-dependent differential repair in the 10*S* (+) isomer. The most plausible factor contributing to the enhanced NER excision activity of the 10*S* (+) adduct in the CA*C sequence (Figure 6) is the possibility for enhanced roll with a significant bend, stabilized by a sequence specific hydrogen bond in the *anti* glycosidic conformation (Table S2 and Figures 3 and 4). The *syn* glycosidic conformer with its disrupted Watson−Crick hydrogen bonding is a component of the conformational equilibrium in both sequences and hence would not account for the sequence-dependent differential NER. However, it does play a role in the differential excision of the *S* and *R* stereoisomers of the same sequence, since a *syn* conformer plays little role in the *R* isomer conformational mix. Our computed greater distortion free energy for the *S* isomer (Table S1) is in line with its higher excision susceptibility, and relates to structural differences in *S* and *R* isomers involving the quality of Watson−Crick hydrogen bonding, unwinding, and roll bending (Table S2). Moreover, recent work has shown a correlation between this distortion energy index and the observed NER efficiencies of intercalated adducts for a number of cases (*37*). The 10*R* (−) adducts behave quite similarly in our simulations for the two sequences, and more similar susceptibilities to NER are suggested by the data. Of course, repair is a complex process governed by a combination of factors, which we term a multipartite model for recognition (*37*, *93*).

Moreover, at the current state of the art it is not feasible to quantitatively relate computed free energies with relative rates of excision through kinetic theory, where a 1 kcal/mol energy difference converts to an ~9-fold rate difference, since uncertainty in the computed free energies is on the order of several kilocalories per mole in systems of the type examined here (*38*). In addition, there is the well-known sampling problem in molecular dynamics simulations, which is still the key limitation to ensuring that important regions of conformational space are well-traversed (*94*); nonetheless, much insightful information is being gained, and the technique is now taken to be a valuable partner to experiment (*95*).

Future experimental studies are needed to further examine these suggestions of sequence dependence in NER, including the possibility of next nearest neighbor effects. It is of interest that sequence-dependent differential repair has also recently been observed in the case of the hypoxanthine and 1,N^6-ethenoadenine−DNA adducts (*96*). Sequence- and stereoisomer-dependent NER could play a role in producing adduct-induced mutational hotspots and thereby contribute to the complexity of cancer initiation.

ACKNOWLEDGMENT

We thank Prof. Robert Shapiro for helpful discussions. Computations were carried out at the National Science Foundation San Diego Supercomputer Center (San Diego, CA), the National Science Foundation Advanced Computing Center for Engineering and Science at the University of Texas at Austin (Austin, TX), and the U.S. Department of Energy National Energy Research Scientific Computing Center. Our own SGI workstations, as well as those of the Information Technology Services at New York University, were used for visualization, modeling, and data analysis.

SUPPORTING INFORMATION AVAILABLE

Table S1 shows the distortion free energy analysis of the 10*S* (+) and 10*R* (−) adducts in the CA*C sequence context. Table S2 shows the comparison of structural parameters for CA*C and CA*A sequence contexts near the lesion site. Figure S1 shows the rmsd relative to the average structures for the 10*S* (+) adduct *anti* and *syn* conformers, the 10*R* (−) adduct, and the unmodified control structure over the 2.5 ns MD simulation. Figure S2 shows the Watson−Crick hydrogen bond angles and distances for the A*6−T17 base pair of the 10*S* (+) adduct *anti* conformer. Figures S3 and S4 show the trajectory average helicoidal and backbone parameters, respectively. Figure S5 shows the overall axis bend of the 10*S* (+) adduct *anti* and *syn* conformers, the 10*R* (−) adduct, and the unmodified control structure over the 2.5 ns MD simulation. Figure S6 shows a stereoview of the *syn* glycosidic conformation of the 10*S* (+) adduct in the CA*A sequence. Figure S7 shows the time dependence of the pseudorotation phase angle *P* for C5 of the 10*S* (+) adduct *anti* conformer. This material is available free of charge via the Internet at http://pubs.acs.org.

REFERENCES

1. Hanrahan, C. J., Bacolod, M. D., Vyas, R. R., Liu, T., Geacintov, N. E., Loechler, E. L., and Basu, A. K. (1997) Sequence specific mutagenesis of the major (+)-*anti*-benzo[*a*]pyrene diol epoxide-DNA adduct at a mutational hot spot in vitro and in *Escherichia coli* cells, *Chem. Res. Toxicol. 10*, 369−377.
2. Alekseyev, Y. O., and Romano, L. J. (2002) Effects of benzo[*a*]-pyrene adduct stereochemistry on downstream DNA replication in vitro: evidence for different adduct conformations within the active site of DNA polymerase I (Klenow fragment), *Biochemistry 41*, 4467−4479.
3. Shukla, R., Liu, T., Geacintov, N. E., and Loechler, E. L. (1997) The major, N^2-dG adduct of (+)-*anti*-B[*a*]PDE shows a dramatically different mutagenic specificity (predominantly, G → A) in a 5′-CGT-3′ sequence context, *Biochemistry 36*, 10256−10261.
4. Shukla, R., Geacintov, N. E., and Loechler, E. L. (1999) The major, N^2-dG adduct of (+)-*anti*-B[*a*]PDE induces G → A mutations in a 5′-AGA-3′ sequence context, *Carcinogenesis 20*, 261−268.
5. Page, J. E., Zajc, B., Oh-hara, T., Lakshman, M. K., Sayer, J. M., Jerina, D. M., and Dipple, A. (1998) Sequence context profoundly influences the mutagenic potency of *trans*-opened benzo[*a*]pyrene 7,8-diol 9,10-epoxide-purine nucleoside adducts in site-specific mutation studies, *Biochemistry 37*, 9127−9137.
6. Ponten, I., Waters, L. S., Sayer, J. M., Pilcher, A. S., Dipple, A., and Jerina, D. M. (2001) Influence of adduct position and sequence length on the ligation of oligonucleotides containing benzo[*c*]-phenanthrene diol epoxide-deoxyadenosine adducts into M13mp7L2, *Mutagenesis 16*, 65−69.
7. Seo, K. Y., Jelinsky, S. A., and Loechler, E. L. (2000) Factors that influence the mutagenic patterns of DNA adducts from chemical carcinogens, *Mutat. Res. 463*, 215−246.
8. Bigger, C. A., Ponten, I., Page, J. E., and Dipple, A. (2000) Mutational spectra for polycyclic aromatic hydrocarbons in the *supF* target gene, *Mutat. Res. 450*, 75−93.
9. Ponten, I., Sayer, J. M., Pilcher, A. S., Yagi, H., Kumar, S., Jerina, D. M., and Dipple, A. (1999) Sequence context effects on mutational properties of *cis*-opened benzo[*c*]phenanthrene diol epoxide-deoxyadenosine adducts in site-specific mutation studies, *Biochemistry 38*, 1144−1152.

10. Goodman, M. F. (2002) Error-prone repair DNA polymerases in prokaryotes and eukaryotes, *Annu. Rev. Biochem. 71*, 17−50.
11. Friedberg, E. C., Wagner, R., and Radman, M. (2002) Specialized DNA polymerases, cellular survival, and the genesis of mutations, *Science 296*, 1627−1630.
12. Wagner, J., Etienne, H., Janel-Bintz, R., and Fuchs, R. P. P. (2002) Genetics of mutagenesis in *E. coli*: various combinations of translesion polymerases (Pol II, IV and V) deal with lesion/sequence context diversity, *DNA Repair 1*, 159−167.
13. Chary, P., Latham, G. J., Robberson, D. L., Kim, S. J., Han, S., Harris, C. M., Harris, T. M., and Lloyd, R. S. (1995) *In vivo* and *in vitro* replication consequences of stereoisomeric benzo[*a*]-pyrene-7,8-dihydrodiol 9,10-epoxide adducts on adenine N^6 at the second position of *N-ras* codon 61, *J. Biol. Chem. 270*, 4990−5000.
14. Chary, P., and Lloyd, R. S. (1995) *In vitro* replication by prokaryotic and eukaryotic polymerases on DNA templates containing site-specific and stereospecific benzo[*a*]pyrene-7,8-dihydrodiol-9,10-epoxide adducts, *Nucleic Acids Res. 23*, 1398−1405.
15. Zhuang, P., Kolbanovskiy, A., Amin, S., and Geacintov, N. E. (2001) Base sequence dependence of in vitro translesional DNA replication past a bulky lesion catalyzed by the *exo*-Klenow fragment of Pol I, *Biochemistry 40*, 6660−6669.
16. Rechkoblit, O., Zhang, Y., Guo, D., Wang, Z., Amin, S., Krzeminsky, J., Louneva, N., and Geacintov, N. E. (2002) Translesion synthesis past bulky benzo[*a*]pyrene diol epoxide N^2-dG and N^6-dA lesions catalyzed by DNA bypass polymerases, *J. Biol. Chem. 277*, 30488−30494.
17. Frank, E. G., Sayer, J. M., Kroth, H., Ohashi, E., Ohmori, H., Jerina, D. M., and Woodgate, R. (2002) Translesion replication of benzo[*a*]pyrene and benzo[*c*]phenanthrene diol epoxide adducts of deoxyadenosine and deoxyguanosine by human DNA polymerase iota, *Nucleic Acids Res. 30*, 5284−5292.
18. Shen, X., Sayer, J. M., Kroth, H., Ponten, I., O'Donnell, M., Woodgate, R., Jerina, D. M., and Goodman, M. F. (2002) Efficiency and accuracy of SOS-induced DNA polymerases replicating benzo[*a*]pyrene-7,8-diol-9,10-epoxide A and G adducts, *J. Biol. Chem. 277*, 5265−5274.
19. Weinberg, R. A. (1996) How cancer arises, *Sci. Am. 275*, 62−70.
20. Garner, R. C. (1998) The role of DNA adducts in chemical carcinogenesis, *Mutat. Res. 402*, 67−75.
21. Kozack, R., Seo, K. Y., Jelinsky, S. A., and Loechler, E. L. (2000) Toward an understanding of the role of DNA adduct conformation in defining mutagenic mechanism based on studies of the major adduct (formed at N^2-dG) of the potent environmental carcinogen, benzo[*a*]pyrene, *Mutat. Res. 450*, 41−59.
22. Geacintov, N. E., Cosman, M., Hingerty, B. E., Amin, S., Broyde, S., and Patel, D. J. (1997) NMR solution structures of stereoisometric covalent polycyclic aromatic carcinogen-DNA adduct: principles, patterns, and diversity, *Chem. Res. Toxicol. 10*, 111−146.
23. Patel, D. J., Mao, B., Gu, Z., Hingerty, B. E., Gorin, A., Basu, A. K., and Broyde, S. (1998) Nuclear magnetic resonance solution structures of covalent aromatic amine-DNA adducts and their mutagenic relevance, *Chem. Res. Toxicol. 11*, 391−407.
24. Conney, A. H. (1982) Induction of microsomal enzymes by foreign chemicals and carcinogenesis by polycyclic aromatic hydrocarbons: G. H. A. Clowes memorial lecture, *Cancer Res. 42*, 4875−4917.
25. Cheng, S. C., Hilton, B. D., Roman, J. M., and Dipple, A. (1989) DNA adducts from carcinogenic and noncarcinogenic enantiomers of benzo[*a*]pyrene dihydrodiol epoxide, *Chem. Res. Toxicol. 2*, 334−340.
26. Meehan, T., and Straub, K. (1979) Double-stranded DNA stereoselectively binds benzo[*a*]pyrene diol epoxides, *Nature 277*, 410−412.
27. Szeliga, J., and Dipple, A. (1998) DNA adduct formation by polycyclic aromatic hydrocarbon dihydrodiol epoxides, *Chem. Res. Toxicol. 11*, 1−11.
28. Fountain, M. A., and Krugh, T. R. (1995) Structural characterization of a (+)-*trans*-*anti*-benzo[*a*]pyrene-DNA adduct using NMR, restrained energy minimization, and molecular dynamics, *Biochemistry 34*, 3152−3161.
29. Xu, R., Mao, B., Amin, S., and Geacintov, N. E. (1998) Bending and circularization of site-specific and stereoisomeric carcinogen-DNA adducts, *Biochemistry 37*, 769−778.
30. Schwartz, J. L., Rice, J. S., Luxon, B. A., Sayer, J. M., Xie, G., Yeh, H. J. C., Liu, X., Jerina, D. M., and Gorenstein, D. G. (1997) Solution structure of the minor conformer of a DNA duplex containing a dG mismatch opposite a benzo[*a*]pyrene diol epoxide/dA adduct: glycosidic rotation from *syn* to *anti* at the modified deoxyadenosine, *Biochemistry 36*, 11069−11076.
31. Yeh, H. J., Sayer, J. M., Liu, X., Altieri, A. S., Byrd, R. A., Lakshman, M. K., Yagi, H., Schurter, E. J., Gorenstein, D. G., and Jerina, D. M. (1995) NMR solution structure of a nonanucleotide duplex with a dG mismatch opposite a 10*S* adduct derived from *trans* addition of a deoxyadenosine N^6-amino group to (+)-(7*R*,8*S*,9*S*,10*R*)-7,8-dihydroxy-9,10-epoxy-7,8,9,10-tetrahydrobenzo[*a*]pyrene: an unusual *syn* glycosidic torsion angle at the modified dA, *Biochemistry 34*, 13570−13581.
32. Zegar, I. S., Chary, P., Jabil, R. J., Tamura, P. J., Johansen, T. N., Lloyd, R. S., Harris, C. M., Harris, T. M., and Stone, M. P. (1998) Multiple conformations of an intercalated (−)-(7*S*,8*R*,9*S*,10*R*)-N^6-[10-(7,8,9,10-tetrahydrobenzo[*a*]pyrenyl)]-2′-deoxyadenosyl adduct in the *N-ras* codon 61 sequence, *Biochemistry 37*, 16516−16528.
33. Volk, D. E., Rice, J. S., Luxon, B. A., Yeh, H. J. C., Liang, C., Xie, G., Sayer, J. M., Jerina, D. M., and Gorenstein, D. G. (2000) NMR evidence for *syn-anti* interconversion of a *trans* opened (10*R*)-dA adduct of benzo[*a*]pyrene (7*S*,8*R*)-diol (9*R*,10*S*)-epoxide in a DNA duplex, *Biochemistry 39*, 14040−14053.
34. Zegar, I. S., Kim, S. J., Johansen, T. N., Horton, P. J., Harris, C. M., Harris, T. M., and Stone, M. P. (1996) Adduction of the human *N-ras* codon 61 sequence with (−)-(7*S*,8*R*,9*R*,10*S*)-7,8-dihydroxy-9,10-epoxy-7,8,9,10-tetrahydrobenzo[*a*]pyrene: structural refinement of the intercalated SRSR(61,2) (−)-(7*S*,8*R*,9*S*,10*R*)-N^6-[10-(7,8,9,10-tetrahydrobenzo[*a*]pyrenyl)]-2′-deoxyadenosyl adduct from ^{1}H NMR, *Biochemistry 35*, 6212−6224.
35. Mao, B., Gu, Z., Gorin, A., Chen, J., Hingerty, B. E., Amin, S., Broyde, S., Geacintov, N. E., and Patel, D. J. (1999) Solution structure of the (+)-*cis*-*anti*-benzo[*a*]pyrene-dA ([BP]dA) adduct opposite dT in a DNA duplex, *Biochemistry 38*, 10831−10842.
36. Yan, S., Shapiro, R., Geacintov, N. E., and Broyde, S. (2001) Stereochemical, structural and thermodynamic origins of stability differences between stereoisomeric benzo[*a*]pyrene diol epoxide deoxyadenosine adducts in a DNA mutational hot spot sequence, *J. Am. Chem. Soc. 123*, 7054−7066.
37. Wu, M., Yan, S., Patel, D. J., Geacintov, N. E., and Broyde, S. (2002) Relating repair susceptibility of carcinogen-damaged DNA with structural distortion and thermodynamic stability, *Nucleic Acids Res. 30*, 3422−3432.
38. Yan, S., Wu, M., Patel, D. J., Geacintov, N. E., and Broyde, S. (2003) Simulating structural and thermodynamic properties of carcinogen-damaged DNA, *Biophys. J.* (in press).
39. Buterin, T., Hess, M. T., Luneva, N., Geacintov, N. E., Amin, S., Kroth, H., Seidel, A., and Naegeli, H. (2000) Unrepaired fjord region polycyclic aromatic hydrocarbon-DNA adducts in *ras* codon 61 mutational hot spots, *Cancer Res. 60*, 1849−1856.
40. Berman, H. M., Westbrook, J., Feng, Z., Gilliland, G., Bhat, T. M., Weissig, H., Shindyalov, I. N., and Bourne, P. E. (2000) The protein data bank, *Nucleic Acids Res. 28*, 235−242.
41. Hingerty, B. E., Figueroa, S., Hayden, T. L., and Broyde, S. (1989) Prediction of DNA structure from sequence: a build-up technique, *Biopolymers 28*, 1195−1222.
42. Arnott, S., Smith, P. J. C., and Chandrasekaran, R. (1976) *Handbook of Biochemistry and Molecular Biology*, 3rd ed., pp 411−422, CRC Press, Cleveland, OH.
43. Schurter, E. J., Yeh, H. J., Sayer, J. M., Lakshman, M. K., Yagi, H., Jerina, D. M., and Gorenstein, D. G. (1995) NMR solution structure of a nonanucleotide duplex with a dG mismatch opposite a 10*R* adduct derived from *trans* addition of a deoxyadenosine N^6-amino group to (−)-(7*S*,8*R*,9*R*,10*S*)-7,8-dihydroxy-9,10-epoxy-7,8,9,10-tetrahydrobenzo[*a*]pyrene, *Biochemistry 34*, 1364−1375.
44. Frisch, M. J., Trucks, G. W., Schlegel, H. B., Gill, P., Johnsone, B. G., Robb, M. A., Cheeseman, J. R., Keith, T. A., Petersson, G. A., Montgomery, J. A., Raghavachari, K., Al-Laham, M. A., Zakrzewski, V. G., Ortiz, J. V., Foresman, J. B., Cioslowski, J., Stefanov, B. B., Nanayakkara, A., Challacombe, M., Peng, C. Y., Ayala, P. Y., Chen, W., Wong, M. W., Andres, J. L., Reploge, E. S., Gomperts, R., Martin, R. L., Fox, D. J., Binkley, J. S., Defrees, D. J., Baker, J., Stewart, J. P., Head-Gordon, M., Gonzalez, C., and Pople, J. A. (1995) *Gaussian 94*, Revision A.1, Gaussian, Inc., Pittsburgh, PA.
45. Bayly, C. I., Cieplak, P., Cornell, W. D., and Kollman, P. A. (1993) A well-behaved electrostatic potential based method using charge restraints for deriving atomic charges: the RESP model, *J. Phys. Chem. 97*, 10269−10280.

46. Wu, X., Shapiro, R., and Broyde, S. (1999) Conformational analysis of the major DNA adduct derived from the food mutagen 2-amino-3-methylimidazo[4,5-*f*]quinoline, *Chem. Res. Toxicol. 12*, 895−905.
47. Cheatham, T. E., Cieplak, P., and Kollman, P. A. (1999) A modified version of the Cornell *et al*. force field with improved sugar pucker phases and helical repeat, *J. Biomol. Struct. Dyn. 16*, 845−862.
48. Case, D. A., Pearlman, D. A., Caldwell, J. W., Cheatham, T. E., Ross, W. S., Simmerling, C. L., Darden, T. A., Merz, K. M., Stanton, R. V., Cheng, A. L., Vincent, J. J., Crowley, M., Ferguson, D. M., Radmer, R. J., Seibel, G. L., Singh, U. C., Weiner, P. K., and Kollman, P. A. (1997) *AMBER 5.0*, University of California, San Francisco.
49. Cornell, W. D., Cieplak, P., Bayly, C. I., Gould, I. R., Merz, K. M., Ferguson, D. M., Spellmeyer, D. C., Fox, T., Caldwell, J. W., and Kollman, P. A. (1995) A second generation force field for the simulation of proteins, nucleic acids, and organic molecules, *J. Am. Chem. Soc. 117*, 5179−5197.
50. Darden, T., York, D., and Pedersen, L. (1993) Particle mesh Ewald: an *N*·log(*N*) method for Ewald sums in large systems, *J. Chem. Phys. 98*, 10089−10092.
51. Essmann, U., Perera, L., Berkowitz, M. L., Darden, T., Lee, H., and Pederson, L. G. (1995) A smooth particle mesh Ewald method, *J. Chem. Phys. 103*, 8577−8593.
52. Ryckaert, J. P., Ciccotti, G., and Berendsen, H. J. C. (1977) Numerical integration of cartesian equations of motion of a system with constraints: molecular dynamics of *n*-alkanes, *J. Comput. Phys. 23*, 327−341.
53. Harvey, S. C., Tan, R. K.-Z., and Cheatham, T. E. (1998) The flying ice cube: velocity rescaling in molecular dynamics leads to violation of energy equipartition, *J. Comput. Chem. 19*, 726−740.
54. Jorgensen, W. L., Chandreskhar, J., Madura, J. D., Imprey, R. W., and Klein, M. L. (1983) Comparison of simple potential functions for simulating liquid water, *J. Chem. Phys. 79*, 926−935.
55. Berendsen, H. J. C., Postma, J. P. M., vanGunsteren, W. F., DiNola, A., and Haak, J. R. (1984) Molecular dynamics with coupling to an external bath, *J. Chem. Phys. 81*, 3684−3690.
56. Ravishanker, G., Swaminathan, S., Beveridge, D. L., Lavery, R., and Sklenar, H. (1989) Conformational and helicoidal analysis of 30 ps of molecular dynamics on the d(CGCGAATTCGCG) double helix: "curves", dials and windows, *J. Biomol. Struct. Dyn. 6*, 669−699.
57. Simmerling, C., Elber, R., and Zhang, J. (1995) *Modelling of Biomolecular Structure and Mechanisms*, pp 241−265, Kluwer, Dordrecht, The Netherlands.
58. Lavery, R., and Sklenar, H. (1988) The definition of generalized helicoidal parameters and of axis curvature for irregular nucleic acids, *J. Biomol. Struct. Dyn. 6*, 63−91.
59. Nicholls, A., Sharp, K. A., and Honig, B. (1990) *DelPhi*, Department of Biochemistry and Molecular Biophysics, Columbia University, New York.
60. Honig, B., and Nicholls, A. (1995) Classical electrostatics in biology and chemistry, *Science 268*, 1144−1149.
61. Sanner, M. F., Olson, A. J., and Spehner, J. C. (1996) Reduced surface: an efficient way to compute molecular surfaces, *Biopolymers 38*, 305−320.
62. Srinivasan, J., Cheatham, T. E., Cieplak, P., Kollman, P. A., and Case, D. A. (1998) Continuum solvent studies of the stability of DNA, RNA, and phosphoramidate-DNA helices, *J. Am. Chem. Soc. 120*, 9401−9409.
63. Steinbrecher, T., Becker, A., Stezowski, J. J., Oesch, F., and Seidel, A. (1993) Synthesis of oligodeoxynucleotides containing diastomeric diol epoxide-N^6-deoxyadenosine adducts of polycyclic aromatic hydrocarbons, *Tetrahedron Lett. 34*, 1773−1774.
64. Kroth, H., Oesch, F., and Seidel, A. (1996) Synthesis of stereoisomeric N^6-deoxyadenosine adducts of *syn*- and *anti*-dihydrodiol epoxides of benzo[*a*]pyrene and their incorporation into 18-mer DNA sequences from human Ha-*ras* proto-oncogene, *Polycyclic Aromat. Compd. 11*, 349−356.
65. Laryea, A., Cosman, M., Lin, J.-M., Liu, T., Agarwal, R., Smirnov, S., Amin, S., Harvey, R. G., Dipple, A., and Geacintov, N. E. (1995) Direct synthesis and characterization of site-specific adenosyl adducts derived from the binding of a 3,4-dihydroxy-1,2-epoxybenzo[*c*]phenanthrene stereoisomer to an 11-mer oligodeoxyribonucleotide, *Chem. Res. Toxicol. 8*, 444−454.
66. Ni, J., Liu, T., Kolbanovskiy, A., Krzeminski, J., Amin, S., and Geacintov, N. E. (1998) Mass spectrometric sequencing of site-specific carcinogen-modified oligodeoxyribonucleotides containing bulky benzo[*a*]pyrene diol epoxide-deoxyguanosyl adducts, *Anal. Biochem. 264*, 222−229.
67. Huang, J.-C., Hsu, D. S., Kazantsev, A., and Sancar, A. (1994) Substrate spectrum of human excinuclease: repair of abasic sites, methylated bases, mismatches, and bulky adducts, *Proc. Natl. Acad. Sci. U.S.A. 91*, 12213−12217.
68. Matsunaga, T., Mu, D., Park, C.-H., Reardon, J. T., and Sancar, A. (1995) Human DNA repair excision nuclease, *J. Biol. Chem. 270*, 20862−20869.
69. Hess, M. T., Schwitter, U., Petretta, M., Giese, B., and Naegeli, H. (1997) Bipartite substrate discrimination by human nucleotide excision repair, *Proc. Natl. Acad. Sci. U.S.A. 94*, 6664−6669.
70. Pradhan, P., Tirumala, S., Liu, X., Sayer, J. M., Jerina, D. M., and Yeh, H. J. C. (2001) Solution structure of a *trans*-opened (10*S*)-dA adduct of (+)-(7*S*,8*R*,9*S*,10*R*)-7,8-dihydroxy-9,10-epoxy-7,8,9,10-tetrahydrobenzo[*a*]pyrene in a fully complementary DNA duplex: evidence for a major *syn* conformation, *Biochemistry 40*, 5870−5881.
71. Berman, H. M. (1997) Crystal studies of B-DNA: the answers and the questions, *Biopolymers 44*, 23−44.
72. Saenger, W. (1984) *Principles of Nucleic Acid Structure*, Springer-Verlag, New York.
73. Olson, W. K., Bansal, M., Burley, S. K., Dickerson, R. E., Gerstein, M., Harvey, S. C., Heinemann, U., Lu, X. J., Neidle, S., Shakked, Z., Sklenar, H., Suzuki, M., Tung, C. S., Westhof, E., Wolberger, C., and Berman, H. M. (2001) A standard reference frame for the description of nucleic acid base-pair geometry, *J. Mol. Biol. 313*, 229−237.
74. Lu, X. J., and Olson, W. K. (1999) Resolving the discrepancies among nucleic acid conformational analyses, *J. Mol. Biol. 285*, 1563−1575.
75. Dickerson, R. E. (1998) DNA bending: the prevalence of kinkiness and the virtues of normality, *Nucleic Acids Res. 26*, 1906−1926.
76. Krzeminski, J., Ni, J., Zhuang, P., Luneva, N., Amin, S., and Geacintov, N. E. (1999) Total synthesis, mass spectrometric sequencing, and stabilities of oligonucleotide duplexes with single *trans-anti*-BPDE-N^6-dA lesions in the *N-ras* codon 61 and other sequence contexts, *Polycyclic Aromat. Compd. 17*, 1−10.
77. Lakshminarayanan, A. V., and Sasisekharan, V. (1969) Stereochemistry of nucleic acids and polynucleotides 4. Conformational energy of base-sugar units, *Biopolymers 8*, 475−488.
78. Olson, W. K. (1973) *Syn-anti* effects on spatial configuration of polynucleotide chains, *Biopolymers 12*, 1787−1814.
79. Yathindra, N., and Sundaralingam, M. (1973) Correlation between backbone and side-chain conformations in 5′-nucleotides: concept of a rigid nucleotide conformation, *Biopolymers 12*, 297−314.
80. Schneider, B., Neidle, S., and Berman, H. M. (1997) Conformations of the sugar-phosphate backbone in helical DNA crystal structures, *Biopolymers 42*, 113−124.
81. Berman, H. M. (1997) Crystal studies of B-DNA: the answers and the questions, *Biopolymers 44*, 23−44.
82. Vijay-Kumar, S., Sakore, T. D., and Sobell, H. M. (1984) Structure of a novel drug-nucleic acid crystalline complex: 1,10-phenanthroline-platinum (II) ethylenediamine-5′-phosphoryl-thymidylyl-(3′-5′) deoxyadenosine, *J. Biomol. Struct. Dyn. 2*, 333−344.
83. Wang, A. H., Ughetto, G., Quigley, G. J., and Rich, A. (1987) Interactions between an anthracycline antibiotic and DNA: molecular structure of daunomycin complexed to d(CpGpTpApCpG) at 1.2-Å resolution, *Biochemistry 26*, 1152−1163.
84. Berman, H. M., Neidle, S., and Stodola, R. K. (1978) Drug-nucleic acid interactions: conformational flexibility at the intercalation site, *Proc. Natl. Acad. Sci. U.S.A. 75*, 828−832.
85. Le, P. T. Q., Harris, C. M., Harris, T. M., and Stone, M. P. (2000) Altered electrophoretic migration of polycyclic aromatic hydrocarbon and styrene oxide adducts at adenine N^6 correlates with adduct-induced structural disorder, *Chem. Res. Toxicol. 13*, 63−71.
86. Wood, R. D. (1999) DNA damage recognition during nucleotide excision repair in mammalian cells, *Biochimie 81*, 39−44.
87. Evans, E., Moggs, J. G., Hwang, J. R., Egly, J.-M., and Wood, R. D. (1997) Mechanism of open complex and dual incision formation by human nucleotide excision repair factors, *EMBO J. 16*, 6559−6573.
88. Fujiwara, Y., Masutani, C., Mizukoshi, T., Kondo, J., Hanaoka, F., and Iwai, S. (1999) Characterization of DNA recognition by

the human UV-damaged DNA-binding protein, *J. Biol. Chem. 274*, 20027−20033.
89. Buschta-Hedayat, N., Buterin, T., Hess, M. T., Missura, M., and Naegeli, H. (1999) Recognition of nonhybridizing base pairs during nucleotide excision repair of DNA, *Proc. Natl. Acad. Sci. U.S.A. 96*, 6090−6095.
90. Missura, M., Buterin, T., Hindges, R., Hubscher, U., Kasparkova, J., Brabec, V., and Naegeli, H. (2001) Double-check probing of DNA bending and unwinding by XPA-RPA: an architectural function in DNA repair, *EMBO J. 20*, 3554−3564.
91. Shi, Q., Thresher, R., Sancar, A., and Griffith, J. (1992) Electron microscopic study of (A)BC excinuclease DNA is sharply bent in the UvrB-DNA complex, *J. Mol. Biol. 226*, 425−432.
92. Verhoeven, E. E., Wyman, C., Moolenaar, G., Hoeijmakers, J. H., and Gooseen, N. (2001) Architecture of nucleotide excision repair complexes: DNA is wrapped by UvrB before and after damage recognition, *EMBO J. 20*, 601−611.
93. Geacintov, N. E., Broyde, S., Buterin, T., Naegeli, H., Wu, M., Yan, S., and Patel, D. J. (2002) Thermodynamic and structural factors in the removal of bulky DNA adducts by the nucleotide excision repair machinery, *Biopolymers 65*, 202−210.
94. Cheatham, T. E., and Young, M. A. (2001) Molecular dynamics simulation of nucleic acids: successes, limitations, and promise, *Biopolymers 56*, 232−256.
95. Karplus, M., and McCammon, J. A. (2002) Molecular dynamics simulations of biomolecules, *Nat. Struct. Biol. 9*, 646−652.
96. Wyatt, M. D., and Samson, L. D. (2000) Influence of DNA structure on hypoxanthine and 1,N^6-ethenoadenine removal by murine 3-methyladenine DNA glycosylase, *Carcinogenesis 21*, 901−908.

BI0270081